Non-destructive test system to monitor hydration and strength development of low CO2 concrete

Citation for the original published paper (version of record):
Huang, L., Tang, L., Löfgren, I. et al (2023). Non-destructive test system to monitor hydration and strength development of low CO2 concrete. Construction and Building Materials, 408.
http://dx.doi.org/10.1016/j.conbuildmat.2023.133774

Construction and Building Materials 408 (2023) 133774

Contents lists available at ScienceDirect

Construction and Building Materials

journal homepage: www.elsevier.com/locate/conbuildmat

Non-destructive test system to monitor hydration and strength development of low CO_2 concrete

Liming Huang [a,b,*], Luping Tang [a], Ingemar Löfgren [a,c], Nilla Olsson [d], Arezou Babaahmadi [a], Oskar Esping [c], Yongqiang Li [e], Zhenghong Yang [b]

[a] Department of Architecture and Civil Engineering, Chalmers University of Technology, 41296 Gothenburg, Sweden
[b] Key Laboratory of Advanced Civil Engineering Materials Ministry of Education, Tongji University, Shanghai 201804, PR China
[c] Thomas Concrete Group AB, Södra Vägen 28, 41707 Gothenburg, Sweden
[d] NCC Building, Division Building Sweden, 17080 Solna, Sweden
[e] College of Civil and Transportation Engineering, Shenzhen University, Shenzhen 518060, Guangdong, PR China

ARTICLE INFO

Keywords:
SCMs
Non-destructive test
Formation factor
Setting
Compressive strength

ABSTRACT

Application of supplementary cementitious materials for production of low CO_2 concrete affects the reaction kinetics, which alters the setting time and strength development. The different early-age behavior is of concern for quality control of concrete. Non-destructive test is very useful for monitoring the quality of low CO_2 binder systems. This paper presents a new technique to monitor the electrical conductivity and temperature at different depths of hydrating concrete. Indices from monitoring system (conductivity, maturity and formation factor) are compared with data from widely-used methods (ultrasonic pulse velocity, penetration resistance and isothermal calorimetry). Results show that indices from the system can replicate the hydration evolution, setting time and compressive strength of low CO_2 concrete. Electrical conductivity of concrete is very sensitive to mineral reactions and it reflects the hydration kinetic consistent with evolution of heat release. Linear correlations are found for penetration resistance in relation to ultrasonic pulse velocity, formation factor and maturity, respectively. The effects of binder type and water-to-binder ratio on hardening are strongly dependent on temperature. The proposed approach enables to include all these factors in characterizing the hardening process of concrete onsite. It is shown that formation factor performs better than ultrasonic pulse velocity on indicating the setting process. Formation factor is also a good parameter for quantitative description of compressive strength development, which is independent of the binder types, mixture proportions and curing ages.

1. Introduction

On the way toward carbon neutrality, many kinds of approaches are tried to reduce CO_2 emissions in construction sector. Using supplementary cementitious materials (SCMs) is currently acknowledged as the primary approach to minimize the cement consumption which leads to lower emissions generated due to cement production [1,2]. An incorporation of SCMs makes impact on both the fresh properties (such as, workability, plastic viscosity and yield strength) and the hardening properties (such as setting time and the strength development) [3]. These properties of the blended concretes at the constructing sites are critical for the practical use of alternative binders. Diversity of SCMs results in difficulties in controlling and predicting the performance of low CO_2 concrete.

During the hydration process of binder, the state of concrete will transit from a fluid to the hardened state that governs both the quality and cost of the construction process. For instance, the time for setting and attainment of specific strength affects decisions in terms of the right time for demoulding and for the further construction procedures such as measures to prevent thermal cracks or heat curing requirements for casting in cold seasons. Moreover, the hardening process is also very important for the digital fabrication (3D printing), as Reiter et al. [4] stated that evolution of specific yield stress of concrete is of significance as otherwise the self-weights of the structure can be destructive. For characterizing the hardening properties of paste, the Vicat apparatus is one of representative traditional methods specified in standards, such as EN 196–3 and ASTM C191-08. For the hardening of concrete, a similar method to measure the penetration resistance is proposed in ASTM

---

* Corresponding author at: Department of Architecture and Civil Engineering, Chalmers University of Technology, 41296 Gothenburg, Sweden.
E-mail address: limingh@chalmers.se (L. Huang).

https://doi.org/10.1016/j.conbuildmat.2023.133774
Received 7 June 2023; Received in revised form 3 October 2023; Accepted 9 October 2023

C403/C403M – 05. However, these traditional methods are operated off-site and time-consuming due to the need of following the specified operational manual. These methods are therefore not adequate for the quality control of a fast or automated construction [5]. It is also well-known that hardening is sensitive to temperature changes so the traditional methods need to control the temperature and humidity of the curing environment. However, these conditions are different from the actual field site, especially during the construction of some massive concrete structures [6]. Therefore, a reliable non-destructive testing method with possibility for an automated on-site monitoring, good efficiency and reliable quality, would be very helpful to mitigate the challenges in handling construction with the use of SCMs.

Although there are many non-destructive methods to assess the mechanical performance [7,8] or to identify problems of concrete structure, such as grouting faults [9] or cracks [10], only few of them can be used to obtain time-resolved hardening properties of concrete. Gu et al. [11] embedded piezoelectric transducers into the concrete specimen as actuators and sensors to detect the harmonic response amplitude and tried to correlate the value to the strength development from 1 day up to 1 month. Tawie and Lee [12] verified the feasibility of piezoceramic sensing technique to monitor the strength development by resonant frequency shift. Voigt et al. [13] compared ultrasonic wave reflection and maturity methods on monitoring the strength of Portland cement mortar by relating them to the compressive strength up to 7 days. However, these investigations did not consider the hardening process before final setting. Shimizu [14] found that the electrical conductivity showed a sudden drop during the setting, and Calleja [15] reported that the conductivity change can reflect the setting of hydraulic materials. However, there was no quantitative description between setting time and evolution of conductivity. The setting of oil well cement has been monitored by ultrasonic pulse velocity (UPV) [16], and the theoretical analysis on setting time was further reported by Scherer et al. [17] in relation to the percolation of hydration products during hydration process. However, it seemed that the percolation point occurred earlier than the initial setting time, and there was no further discussion on final setting point or mechanical performance after final setting. Proton nuclear magnetic resonance relaxometry was applied as a method for indicating pastes setting in correlation to water depletion [18], and it seems to be promising as an nondestructive method in lab research but unpractical for onsite application. Poursaee and Weiss [19] used an electrical impedance spectrometer to build an automated test system to monitor the evolution of electrical conductivity of cement paste. The impedance spectroscopy test system in the cited investigation cannot fulfil an onsite application due to the complex setting and expensive price of machine. Moreover, that investigation only provided a concept to illustrate the possibility of using electrical conductivity to monitor performance, but it did not describe any performance index of concrete.

Our previous investigation found that an electrical conductivity monitoring system is very promising to map the hydration induced microstructure change of the blended pastes [20]. A linear correlation has been identified between inflection time of electrical conductivity and setting time. To promote the onsite monitoring of concrete performance, more factors such as casting environment, the presence of aggregate and curing conditions, have been taken into consideration in this study. As such, the monitoring system has been upgraded with sensor arrays, including the ability of determining temperature and electrical conductivity at various depths. Detailed analysis will be given in this paper to verify the credibility of this nondestructive test system to replicate the evolution of hydration and strength development of concretes containing SCMs. The quantitative correlation will be identified between the monitored indices (maturity and formation factor) and the traditional parameters of low CO_2 concrete (penetration resistance, setting time and compressive strength). The hydration heat of two concrete mixes will be compared with their monitored conductivity for revealing the mechanisms of hydration and hardening. Finally, the correlations between setting, compressive strength and formation factor will be discussed from a physical/chemical-mechanism perspective. This investigate not only provides novel understanding of hydration and structure development of concrete but also offers an upgraded system to monitor the setting process and strength development of concretes with various types of binder, through monitoring temperature and electrical properties from cradle to long-term service.

2. Experimental procedures

2.1. Non-destructive monitoring system

2.1.1. Electrical conductivity and temperature

Concretes were cast in container as shown in Fig. 1. The electrical conductivity of concrete was measured by a four-electrode method to minimize the effect of polarization. The arrangement of electrodes at each row was referred to the Wenner configuration [21] (see 4 blue electrodes in Fig. 1). This set-up is an upgraded version based on our previous system [20]. The old version is rather simple with 4 electrodes, so it can only measure small samples and without the consideration of temperature effect. On the array sensors board, one more sensor (red circle in Fig. 1) is added in the end of each raw to measure the temperature, and these sensors have been calibrated with an accuracy of ± 0.2 °C. Multilayer sensors are assembled on a carrier board, which enables the system to measure temperature and electrical conductivity at different depths of large concrete specimens. The invented device for controlling and data recording of the system has a dimension with 15 × 20 × 50 cm, which is portable for onsite test. The measurement was conducted individually at each raw from the top to bottom. The controlling programs of this system was also improved to avoid the mutual influence of different layers, and to minimize the influence of electrode polarization. It takes about 0.1 s to finish one instant measurement. In the first 24 h, the datalogger recorded the data at a 5-min interval. The time interval was switched to 10 mins from 1 day to 7 days. The data at later hydration ages were collected at 14 days and 28 days.

A major improvement in this method is that the effect of temperature on electrical conductivity has been considered. The temperature effect is described by the Arrhenius equation, Eq. (1). The activation energy (E_a

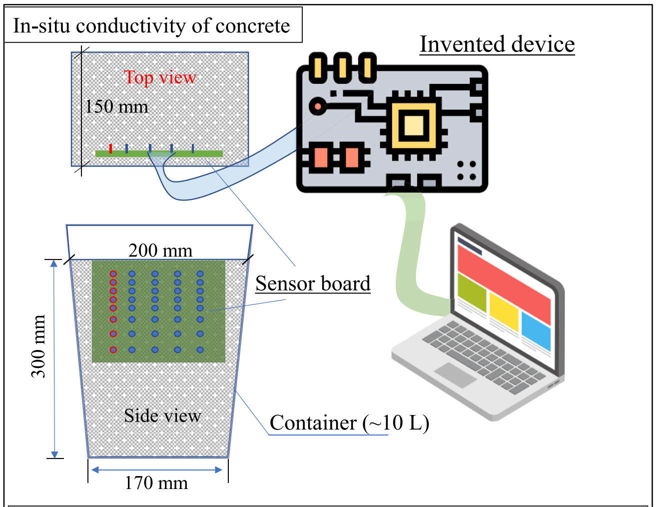

- ○ *Red circles – Temperature sensors*
- ○ *Blue circles – Stainless steel screws, each row as Wenner's 4-electrodes with constant distance of 40 mm*
- ➢ *Sensor array on the board at depth of 10,20,30,40,50,65,80 and 100 mm from the top surface of concrete*

Fig. 1. Setup for monitoring the electrical conductivity and temperature in concrete during hydration.

= 13.375 kJ/mol) was determined by measuring conductivity of the mimic pore solution conditioned between 3 °C and 70 °C. The A is a pre-exponential constant, R is the gas constant (8.314 J / K mol), and T (K) is the absolute temperature of sample.

$$\sigma = A\cdot e^{\frac{E_a}{RT}} \tag{1}$$

The calculation of electrical conductivity by Wenner's method is based on assumption of a semi-infinite boundary. However, the actual size of concrete structure does not always satisfy this semi-infinite boundary condition, especially for the upper rows of the sensors. In order to calibrate the size coefficient on the calculated electrical conductivity, numerical modelling was carried out using COMSOL Multiphysics with a geometry of cuboid (200 × 150 × 300 mm^3) similar as the container (see Fig. 2). The simulation was conducted using the AC/DC mode, which encompassed the electric current conservation equation. Moreover, all surfaces of the geometry were set as insulative boundaries in order to achieve accurate results. The points A and B represent the two outer electrodes in Wenner's configuration. V_2 and V_1 are potential of the inner two electrodes, respectively. The matrix was assigned a constant electrical conductivity of 0.1 mS/cm, and the input constant current from A to B was set to 0.1 mA. The simulated potential difference between V_2 and V_1 was used to calculate the electrical conductivity by Wenner's method. The dimension factor (γ) was evaluated by dividing the given conductivity with the calculated one. Fig. 2 shows that γ is about 1.96 at the first row and decreases with depth. From these simulated results the relationship between γ and the depth of sensors (x) can be established. All these simulated values have been validated with the standard solutions (KCl), and it shows that they are very close to the experimental value (see the comparison of simulated and experimental results in Fig. 2).

After considering effects of both temperature and dimension, the conductivity of hydrating concretes at each depth can be calculated by Eq. (2). The result of each sample in this study is the average value of data from second to eighth row at different depths.

$$\sigma_c = \frac{I}{2\pi\Delta Vd}\cdot\gamma\cdot e^{\frac{Ea}{R}\left(\frac{1}{273.15+T}-\frac{1}{298.15}\right)} \tag{2}$$

where σ_c is electrical conductivity of concretes normalized to 25 °C, I is the applied constant current between the outer two electrodes, ΔV is potential difference between the two middle electrodes, d is the distance between Wenner's electrodes and γ is the dimension factor at different depths.

2.1.2. Ultrasonic pulse velocity

The setup for monitoring UPV (IP-8 Ultrasonic Measuring System

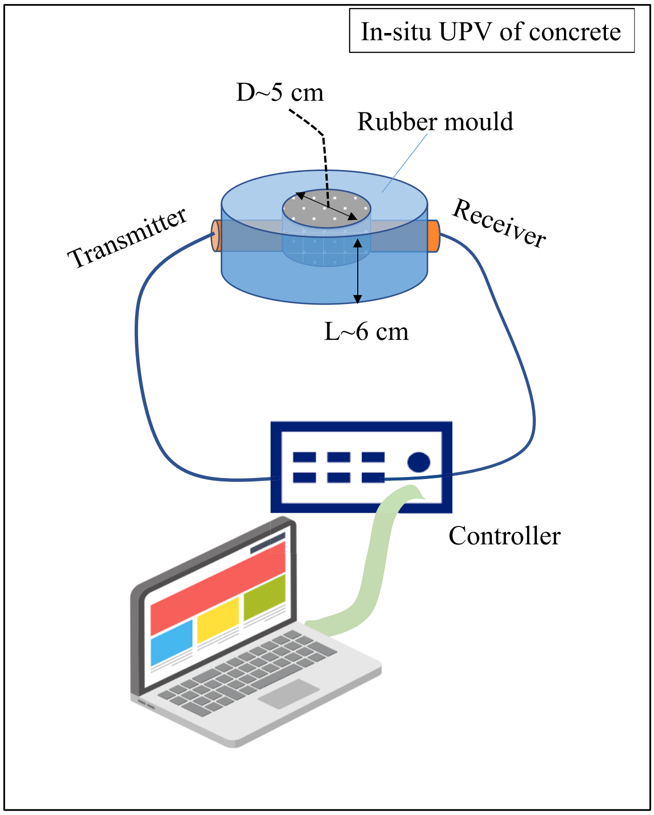

Fig. 3. Setup for monitoring the UPV in concrete during hydration.

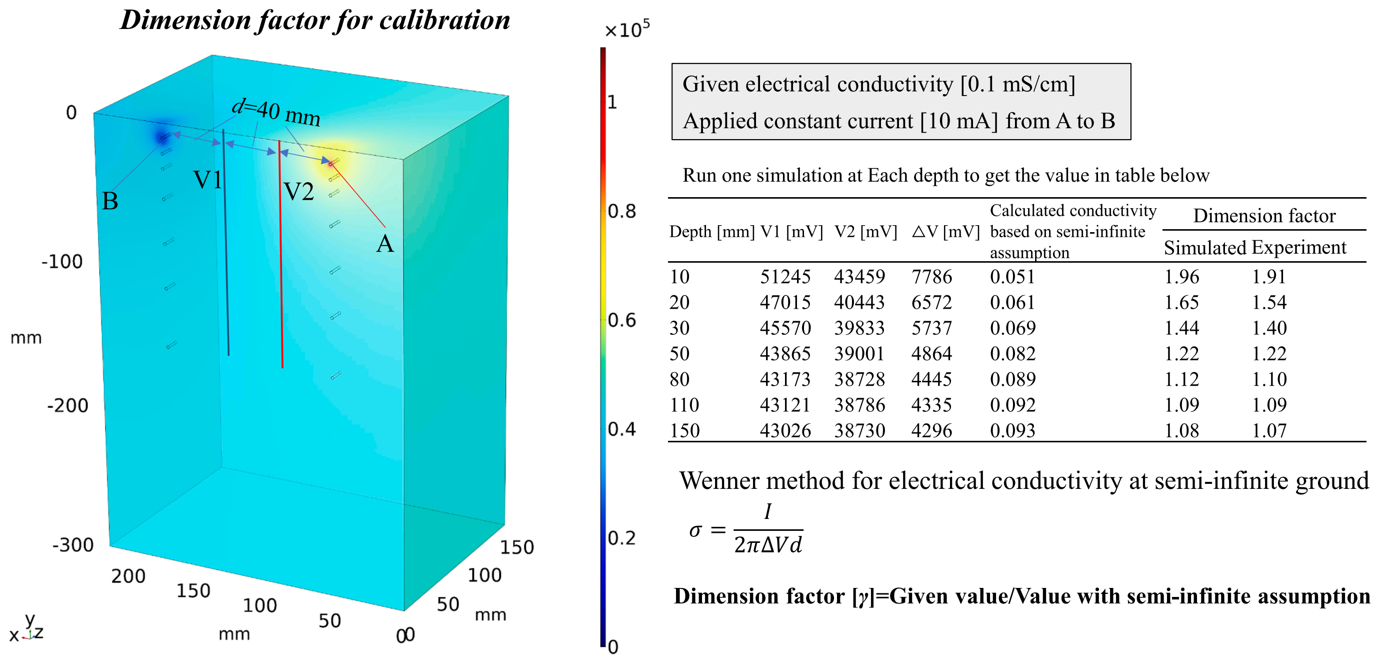

Given electrical conductivity [0.1 mS/cm]
Applied constant current [10 mA] from A to B

Run one simulation at Each depth to get the value in table below

Depth [mm]	V1 [mV]	V2 [mV]	ΔV [mV]	Calculated conductivity based on semi-infinite assumption	Dimension factor	
					Simulated	Experiment
10	51245	43459	7786	0.051	1.96	1.91
20	47015	40443	6572	0.061	1.65	1.54
30	45570	39833	5737	0.069	1.44	1.40
50	43865	39001	4864	0.082	1.22	1.22
80	43173	38728	4445	0.089	1.12	1.10
110	43121	38786	4335	0.092	1.09	1.09
150	43026	38730	4296	0.093	1.08	1.07

Wenner method for electrical conductivity at semi-infinite ground

$$\sigma = \frac{I}{2\pi\Delta Vd}$$

Dimension factor [γ]=Given value/Value with semi-infinite assumption

Fig. 2. Dimension factor based on numerical simulation and comparison with experimental results.

from Ultratest GmbH) is shown in Fig. 3. It consists of two channels with acoustic emission system, a controller and a computer. A transmitter and a receiver are positioned in the silicon mould directly opposite to each other, with a protrusion of approximately 3 mm. This setting aims to ensure a firm connection between the fresh concrete and sensors. The measurement distance between the transmitter and the receiver is 50 mm. The ultrasonic pulse was set with a frequency of 25 kHz. The concrete samples were cast with a mild vibration, and sensor was then connected to the controller under the automatic control of computer. The interval for recording the ultrasonic signal is constant with 2 or 5 min. Each sample had three parallel measurements, and the result is presented as an average value of these measurements.

2.2. Materials

Binders in this study include ordinary Portland cement CEM I 52.5 R with a Blaine surface of 525 m^2/kg, fly ash, and slag with a Blaine surface of 420 m^2/kg. Limestone powder with a $D_{50} = 18$ μm was used as well. The chemical composition of each binder has been shown in the previous paper [20]. Table 1 presents the mix design of 4 kinds of concretes. In the binary systems, the replacement content of cement with slag and fly ash is 35 % by weight. In the ternary systems, Portland cement was replaced with 35 % slag and 16 % limestone. The slag binary concretes were mixed with water-to-binder ratio (*w/b*) of 0.45 (C245) and 0.55 (C255), respectively. The fly ash blended concrete was mixed with *w/b* of 0.45 (C145) and the ternary concrete was mixed with *w/b* of 0.38 (C338). Aggregates used in C145 and C255 consist of siliceous sand and stone with a size distribution ratio of 85.2 %: 14.8 % (1–4 mm: 4–10 mm), which has a bulk density of 1.74×10^3 kg/m^3 and a close packing density of 1.96×10^3 kg/m^3. C245 and C338 were cast using the sand with a density of 2.66×10^3 kg/m^3 from Eurosand and stone with a density of 2.85×10^3 kg/m^3 from Skanska. Superplasticizer (PCE) was Master Glenium 5118 (with 17.5 % dry substance) from Master Builder Solutions.

2.3. Procedures and methods

2.3.1. Casting of concrete

Ingredients of concrete were mixed in a self-falling mixer with capacity of 50 L. Firstly, water and binder were mixed for 2 mins. Subsequently, the aggregates were gradually added into the mixer, and continued to mix for another 5 mins. The fresh concretes were then cast in different containers for monitoring and performance test at certain ages. For monitoring the electrical conductivity and temperature, the board with array sensors was fixed in the container before casting. After filling (with little vibration if needed) to a certain height (10 mm higher than the first row of sensors), the top of the container was sealed to avoid moisture loss. C145 and C255 were cast and cured in climate temperature of 22 ± 1 °C while the production and curing temperature for C245 and C338 was 19 ± 1 °C.

2.3.2. Conductivity of pore solution

The electrical conductivity of pore solution is acquired from data in a previous investigation of pastes with the same cementitious materials. It is assumed that the aggregates are rather stable (for the monitored time), so they do not alter pore solution conductivity and the hydration process. The calculation of pore solution conductivity has been illustrated in [20], which was mainly based on two assumptions: firstly, the alkalis have a fast dissolution within the first few minutes after mixed with water; secondly, the solvent exchanged interlayer water of calcium silicate hydrate is classified as conductive "pore solution".

2.3.3. Setting and strength development

The hardening process of concrete was monitored by a traditional standard (ASTM C 403/C 403 M – 05) with the penetration resistance (strength) test on the mortar part of concrete mixture. After 24 h, concrete cubes were cured in water until the targeted ages. The compressive strength of concrete samples was measured at 12 h, 24 h, 3 days, 7 days, 14 days and 28 days, respectively according to standard EN 12390–3:2019. It should be noted that the size of C145 and C255 sample is $100 \times 100 \times 100$ mm^3, but that of C338 and C245 is $150 \times 150 \times 150$ mm^3. Therefore, the compressive strength values of C145 and C255 were normalized by a dimension factor of 0.93 for a better comparison according to [22].

2.3.4. Isothermal calorimetry

The hydration heat of C245 and C338 was measured by I-Cal 2000 Isothermal Calorimeter (Calmetrix company). It is equipped with 2 sample cells with a capacity of 450 ml. Cells are well isolated from each other by a wide air gap, so it ensures the unparalleled precision and stability by eliminating any cross-influence. The temperature was set to 20 °C with a stability of ± 0.001 °C. Two duplicate measurements were performed simultaneously to obtain an average value for presentative result.

3. Results and discussion

3.1. Real-time monitored data from the upgraded technique

3.1.1. Electrical properties

Fig. 4 shows the real-time monitored electrical properties of hydrating concretes. The formation factor (*F*) of concrete samples is calculated by Eq. (3), where σ_{ps} is the electrical conductivity of pore solution according to [20] and σ_c is the monitored electrical conductivity of concrete. The assumption here is that the siliceous aggregate is rather stable so it does not interact with the pore solution to affect the hydration reactions. It should also be noted that σ_{ps} of C338 is obtained as a multiplicative function of conductivity of paste with *w/b* of 0.35 and a dilution factor (0.38/0.35 = 1.09).

$$F = \frac{\sigma_{ps}}{\sigma_c} \tag{3}$$

Fig. 4a shows that the electrical conductivity of hydrating concrete exhibits a similar trend compared to evolution of electrical conductivity observed in pastes [20]. The upgraded measurement system performs better than the previous version in monitoring hydration before final setting, as it is capable of obtaining a more stable and consistent data line by eliminating polarization effects. In the first 1.8 h, a fast increase in conductivity is caused by a continuous dissolution of clinker [23] and dissolution of slag [24], which results in an increase in pH and alkali concentration. Calcium concentration in pore solution reaches a supersaturated state with respect to portlandite [25]. After this period, the precipitation of hydration products (portlandite and C-S-H) transforms from being dominated by nucleation to growth [26], during which

Table 1
The mixture proportions of concretes (kg/m^3).

Mix ID	Cement	Slag	Fly ash	Limestone	Water	PCE	Sand (<4 mm)	Coarse aggregate (4–10 mm)
C145	286		154		201	3.2	1411	246
C245	280	151			194	3.0	954	795
C255	247	133			209	2.7	1449	256
C338	242	173		79	187	4.0	953	780

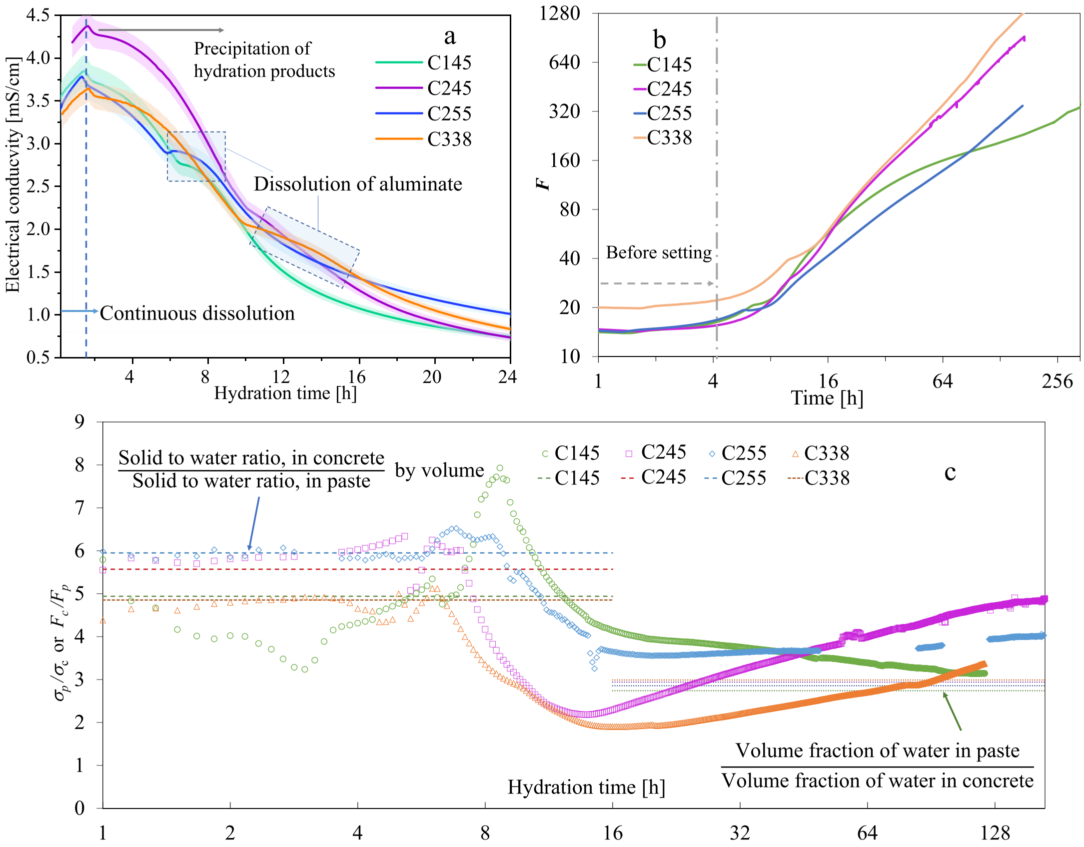

Fig. 4. Real-time monitored electrical properties of concrete: a – evolution of electrical conductivity in the first 24 h; b – the calculated formation factor of concrete: c – the ratio between electrical conductivity of paste and concrete.

period connections are built between mineral particles to reduce the electrical conductivity. In the period from 4 h to 20 h, a peak occurs in all samples. The time for this peak coincides with the second reaction of aluminates in presence of sulfates, which will be later discussed in section 3.3.2. The accelerated dissolution of aluminate and formation of ettringite [27] may reduce the sulfate ion concentration in pore solution so it requires the release of hydroxide ions to balance the charge. This results in a minor increase of conductivity (see C255 in Fig. 4a). The peak for C145 and C255 is observed at approximately 8 h, whereas for C245 and C338 it occurs around 12 h. As pointed out in section 2.2.1, C145 and C255 were cast in a higher environmental temperature compared with C245 and C338. As the peak time of both silicate and aluminate reaction is sensitive to curing temperatures [28,29], the occurrence of the aluminate peak is slower at lower temperature. Conductivity of C245 has the highest value in the first 10 h, whereas the other three mixtures have a similar value when considering the deviation observed in parallel tests.

The dissolution degree of alkalis in fly ash (siliceous fly ash) is much lower than the slag so C145 has a lower alkali concentration and pH than C245 at the same *w/b*. In the period prior to setting, the variation in conductivity of binary concretes is primarily attributable to differences in the concentration of conductive ions present in the pore solution. This is deduced from the fact that the initial formation factors are nearly identical for the binary concretes with a value about 15, as shown in Fig. 4b. The ternary concrete has the highest formation factor over hydration time up to 168 h. This can be ascribed to the lowest effective water to binder ratio, thus introducing the lowest water porosity in concrete matrix. Moreover, the fine limestone can accelerate the hydration [30] and promote an earlier volume-filling hydration process, leading to a denser structure [31]. Its effect is more evident after 32 h according to the increasing difference between C245 and C338. Although the formation factor of C255 is lower than C145 before 86 h due to a higher *w/b*, it grows to be higher than that of fly ash binary concrete as slag involves in the hydration process much earlier than fly ash [32].

The effect of aggregate on the electrical properties is evaluated by dividing formation factor of concrete with that of pastes having the same *w/b*, and this also equals to the ratio between conductivity of pastes and concretes. Fig. 4c shows that incorporation of aggregates will induce a ratio between formation factor of concrete and pastes with a value between 2–7. The value of difference factor before setting time is close to the ratio between the value of solid to water volume ratios in concrete and that of paste. During the hardening process from 6 h to 16 h, the factor has an increase to a peak point and then significantly decreases to value similar with the ratio of water volume fraction in pastes and that of concretes. This implies that the main influential factor shifts from volume of solid to volume of liquid after the percolation of solid networks [17] during the hardening process.

3.1.2. Temperature evolution and maturity

Temperature has a significant effect on the hydration and hardening process of cement-based materials. The temperature of concrete will be affected by two aspects: the environmental temperature and the heat release from the hydration reaction. The latter factor makes major contributions to high temperature in massive concretes. In current research of cement-based materials, an isothermal method is being majorly used to investigate the hydration process and assess hydration degree [33]. However, this kind of isothermal condition is far from the onsite conditions. One advantage of the updated measuring system is to include temperature sensors on the sensor panel for monitoring the temperature regime.

Fig. 5a illustrates the temperature profiles of concretes exposed to the laboratory environment (22 ± 1 °C or 19 ± 1 °C). For the assessment of onsite performance of concretes, an index called maturity [34] was

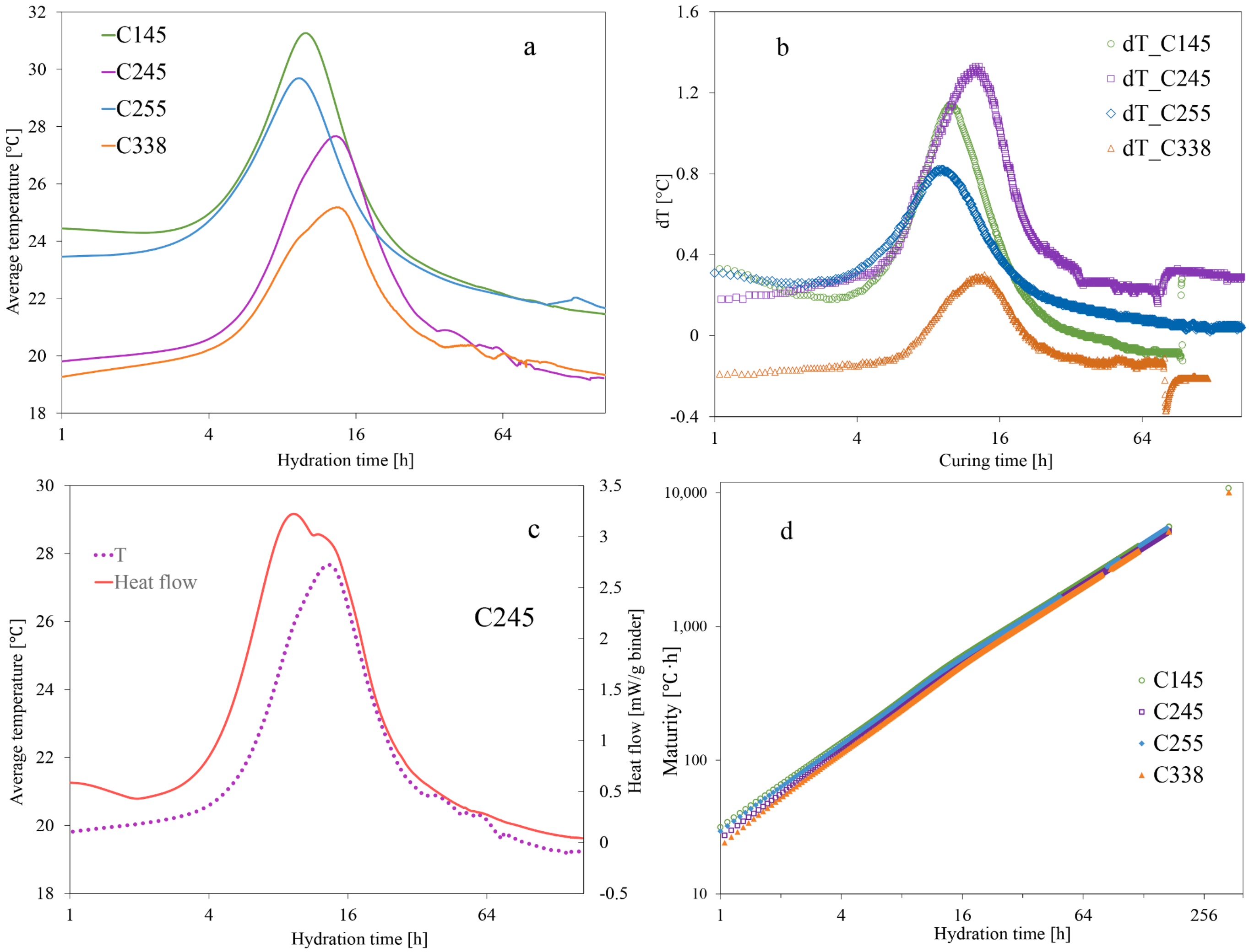

Fig. 5. Monitored temperature evolution and heat release of concretes: a – temperature up to 128 h: b – temperature difference at depth of 100 mm and 10 mm: c – comparison between isothermal calorimetry and temperature evolution of C245: d – maturity of concretes up to 14 days.

defined for assessing the hydration and hardening of concrete. The correlation between maturity and strength (or shrinkage and setting) has been established in many previous investigations [35–38]. Therefore, some nondestructive devices were produced to measure maturity index which can be utilized for assessing the onsite performance of an individual concrete mixture. Maturity index (*M*) of concretes in this study, have been calculated by Eq. (4) according to Nurse-Saul maturity function.

$$M = \sum_{0}^{t} (\overline{T} - T_0)\Delta t \tag{4}$$

where $\overline{T}$ is the average temperature of concretes during the time interval Δt, t is the elapsed time and T_0 is datum temperature for calculation. To evaluate the thermal effect of hydration, the datum temperature is assumed to be −10 °C. The temperature difference (dT) between the inner (at depth of 100 mm) and surface layer (at depth of 10 mm) was evaluated to check the thermal effect of hydration.

The temperatures of the concrete mixes were approximately 1–2 °C higher than the room temperature at starting point (about 12 mins after water mixing) (see Fig. 5a). It stays almost constant at the first 4 h due to a very slow reaction in the induction period. After this period, the temperature reaches a peak due to the heat release from hydration. It starts to decrease after this peak because the heat release rate slows down and becomes lower than heat dissipation rate. Fig. 5b shows that C245 has the maximum temperature difference (about 1.4 °C) between inner part and surface of concrete with the dimensions shown in Fig. 1. The maximum temperature difference for C145, C255 and C338 is 1.2, 0.9 and 0.2 °C, respectively. The occasional negative values are observed in the temperature difference of C338 due to variations in environmental temperature. Fig. 5c demonstrates that the temperature profile in C245 exposed to the lab environment is very close to the heat flow with isothermal calorimetry at 20 °C. An interesting coincidence is that the peak temperature time is simultaneous with the time of aluminate reaction peak. Maturity index of C338 is lowest due to the lowest content of cementitious binder and environmental temperature. C245 has a lower maturity index than C145 in the first day due to a lower curing temperature, but that of C245 grows faster after 4 h because slag has a higher reactivity than fly ash [32,39]. This also explains the higher dT in Fig. 5b. C255 has a higher initial maturity index than C245, but the index of C245 becomes close to C255 after 7 days (168 h).

3.2. Evolution of UPV

Ultrasonic wave velocities in porous materials is determined by the volume fraction of liquid and solid phase [40]. During the hydration of cementitious materials, the changes in connectivity of solid materials also makes impact on the velocity. Hydration induces an increase in rigidity of concrete to increase wave speed, so some investigations have applied the measurement of UPV to indicate the hardening process of cement-based materials [16,17,41,42]. This study used a setup to monitor the evolution of UPV in the hydrating concrete as well.

Fig. 6a shows that UPV of concrete keeps almost constant in the first 2 h because there is little consumption of free water during this period, corresponding to the induction period of cement hydration. UPV of the suspension state is determined by the volume fraction of solid. The ratio between solid and liquid in C145, C245, C255 and C338 is 10.3, 11.1, 9.8 and 11.7, respectively. Consequently, a similar sequence of UPV can be detected in these concretes in the beginning. Some minor differences in the sequence may be caused by the temperature variation. After 2 h the precipitation of hydration products builds solid connections between particles to induce an increase in UPV. The particle connections in C145 grows faster than C255 due to the lower *w/b* [20], so UPV of C145 becomes higher than C255 after 4 h. The square of UPV (v^2) is linearly correlated to elasticity of materials, which is determined by the dynamic Young's modulus and dynamic Poisson ratio [43]. Therefore, the change rate of elasticity can be indicated by the value of $\Delta v^2/\mathrm{d}t$ (see Fig. 6b). It shows that C145 and C338 have a similar tendency of $\Delta v^2/\mathrm{d}t$, and this is consistent with decrease in the connectivity of pore solution as in [20].

As the concrete hardens, the precipitation kinetic of hydration products is decreased, resulting in a decrease in the growth rate of dynamic Young's modulus. From 2 h to 8 h, C255 has the lowest $\Delta v^2/\mathrm{d}t$ due to its highest *w/b*. This can also be attributed to the lower growth rate of solid networks resulting from the dispersed distribution of the precipitated hydration products on particle surface [26,31]. Due to the aluminate reaction from 12 h to 18 h in C245 and C338, there is an evident increase in the growth rate of elasticity. The higher peaks in Fig. 6b implies that the dynamic Young's modulus of C338 increases at a faster rate than C245, which results from acceleration in hydration caused by fine limestone power after 4 h.

3.3. *Properties of setting process*

3.3.1. *Development of penetration resistance*

The penetration resistance was measured by the traditional method (ASTM C403) to indicate the initial hardening process of low carbon concrete. As binders react after water mixing, the nucleation and growth of hydration products cause the formation of clusters which eventually connects into an elastic structural network [17]. During this period, both UPV and formation factor present a significant increase after the solid network reaches a percolation state. Therefore, it is evident that UPV and electrical properties (resistivity and formation factor) can indicate the hydration induced structural development and change of elastic property [44].

Generally, the evolution of penetration resistance has a similar time-dependent tendency as the evolution of both UPV and formation factor (see Fig. 7). According to the definition of initial and final setting in ASTM C403, the development of penetration resistance can be classified into two regions with the initial setting resistance (3.5 MPa) as the critical point. During the setting period, the determining parameter of stress has found to be the interparticle or C-S-H internetwork distance [45], which is affected by the fineness of the particles, *w/b* and reactivity of binders [46]. For pastes cured under the same condition, we have observed that an increase in *w/b* weakens the resistance to needle penetration [20]. Fig. 7 shows that although C245 has a higher value in both UPV and formation factor, the development of penetration resistance is slower than that of C255 in the first 5 h. This is mainly due to the impact of temperature on the hydration and setting [47,48], which is also reflected by the lower maturity index in Fig. 4. To evaluate the effect of temperature on hydration of low carbon concrete, the equivalent curing age (t_e) of concrete was calculated by Eq. (5) [34].

$$t_e = \sum_{0}^{t} e^{-\frac{E}{R}\left(\frac{1}{T}-\frac{1}{T_r}\right)}\Delta t \tag{5}$$

where E is apparent activation energy of hydration (30 kJ/mol for C145 and C255; 44 kJ/mol for C338 and C245 [49]). T_r is the absolute reference temperature (298.15 K).

The equivalent curing age of samples is presented on the upper coordinate axis in Fig. 7. It shows that the growth rate of penetration resistance in C245 and C255 is quite similar before the initial setting, in terms of the equivalent curing age. However, after this time the growth of resistance in C245 (with average of 11.1 MPa/h) is much faster than C255 (with average of 6.7 MPa/h), and it is consistent with the evolution of UPV (see Fig. 6). The fine limestone can provide nucleation sites for hydration products so it can accelerate the hydration of clinker [50]. Moreover, the lower *w/b* induces a shorter particle distance, so these dual effects result in the fastest development of penetration resistance in C338 among all the mixes with respect to equivalent curing age. For the fly ash binary system, aluminate ion from fly ash may hinder the hydration of silicates due to its binding on the surface sites [51]. Therefore, C145 has a slower hardening process than C245 especially after the initial setting. The surface charge and precipitation rate of hydration product on SCMs particle surface is also an important factor controlling the hardening process [52,53]. After initial setting, penetration resistance is determined by the reactivity of the binder and the liquid volume in the mix.

Fig. 8 demonstrates a detailed comparison between hydration heat release, electrical conductivity, UPV, formation factor and penetration resistance with the slag blended concrete as an example. In the left panel of figure, it shows a comparison between the evolution of heat flow and change rate of conductivity. As the heat flow reaches the lowest value at about 2 h, the change rate of electrical conductivity ($\Delta\sigma/\Delta t$) declines

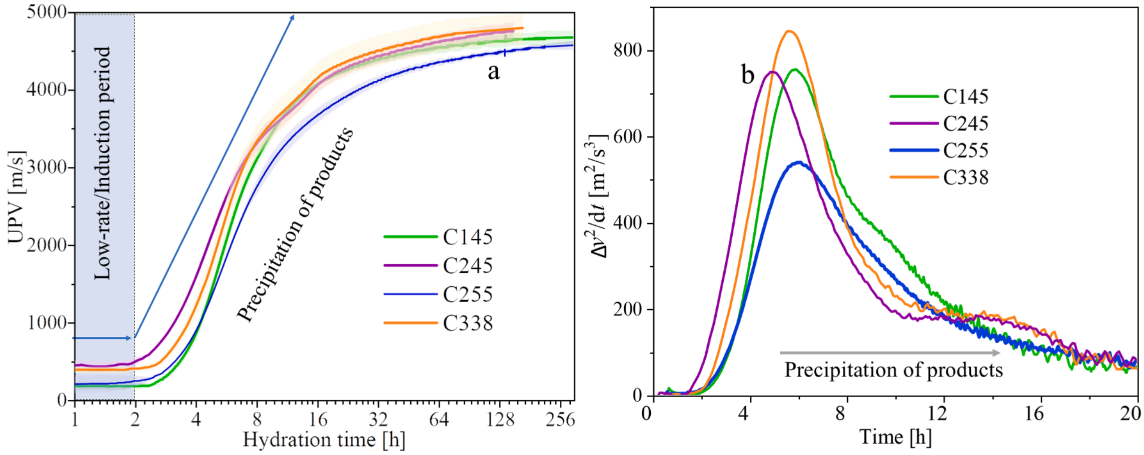

Fig. 6. Monitored UPV in hydrating concrete (a) and $\mathrm{d}v^2/\mathrm{d}t$ (b).

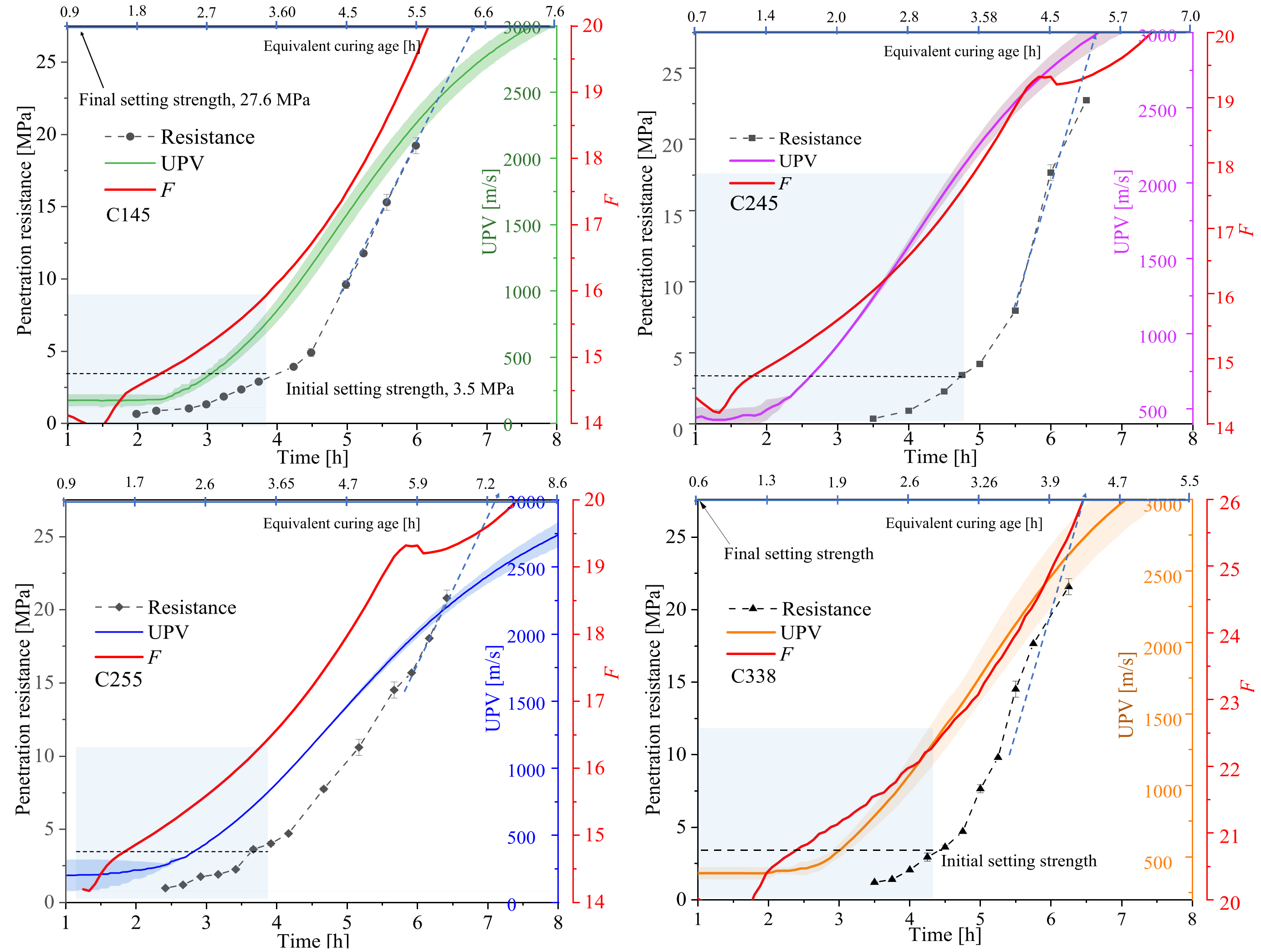

Fig. 7. Evolution of penetration resistance of concretes compared with the UPV and formation factor.

from a positive to a negative value. This means that the dissolution rate of conductive ions largely decreases. Moreover, the reduction in the distance between particles results in the decrease in the connectivity of pore solution [20,54], causing a decrease in conductivity. An intriguing increment in the change rate of conductivity ($\Delta\sigma/\Delta t$) is observed between 2 and 3 h, which can be attributed to an increase in pH during the process of C-S-H growth [23]. After entering the acceleration period of alite hydration, $\Delta\sigma/\Delta t$ shows a sharp decrease. The peak time of the lowest $\Delta\sigma/\Delta t$ is very close to peak of heat flow from the alite hydration. The minor difference is mainly due to a higher temperature in the mixtures cured in a laboratory climate condition in comparison with (see Fig. 4) the samples tested in an isothermal temperature (20 °C).

After the main peak of alite hydration, a further dissolution of C_3A and the accelerated formation of ettringite will induce a aluminate peak [55]. During this period $\Delta\sigma/\Delta t$ increases due to the fact that the aluminate reaction causes an increase in concentration of hydroxide ions. This implies that aluminate peak can also be detected by the electrical conductivity change. The precipitation rate of hydration products gradually decreases as the hydration goes into the deceleration period, so both the heat flow and $\Delta\sigma/\Delta t$ enter a rather stable stage. After the induction period, an increase in penetration resistance is observed, as well as in UPV and formation factor. The hydration heat release has a very low value at both the initial setting and final setting time with about 9 J/g and 20 J/g binder. These values account for less than 5 % of a complete hydration of these binder system (typical heat with 460–470 J/g [56]). The increases in UPV and formation factor are also rather minor compared with the values after 7 days (see Fig. 6). A detailed correlation between penetration resistance and these values will be presented in the next section.

3.3.2. Penetration resistance in relation to UPV, formation factor and maturity

The development of penetration resistance is largely changed after the initial setting, as observed in the previous section. Kolawole et al. [57] applied a shear rheo-viscoelasticity approach to test the properties of concrete mixtures from water mixing to sometime after final setting. They classified the response of mix into 3 kinds of states: (1) plastic state; (2) semi-plastic state; and (3) solid state. These terms are originally defined in soil mechanics by Atterberg, which is called Atterberg limits [58,59] using to correlate the state of soils to moisture content. When penetration resistance is plotted against UPV, formation factor and maturity, the correlations can be classified into two regions: plastic state with resistance value lower than ~ 4.9 MPa and semi-solid (plastic) state between 4.9 MPa and 27.6 MPa. Fig. 9 shows the correlations in these two different states and Table 2 shows the results of regression in two regions separately. According to the R^2 value, a linear correlation can be observed in the relationship between penetration resistance and these three monitored properties, respectively. The slope of the linear line at semi-solid state (k_2) is much lower than that at plastic state (k_1).

During the plastic state, the penetration resistance is actually

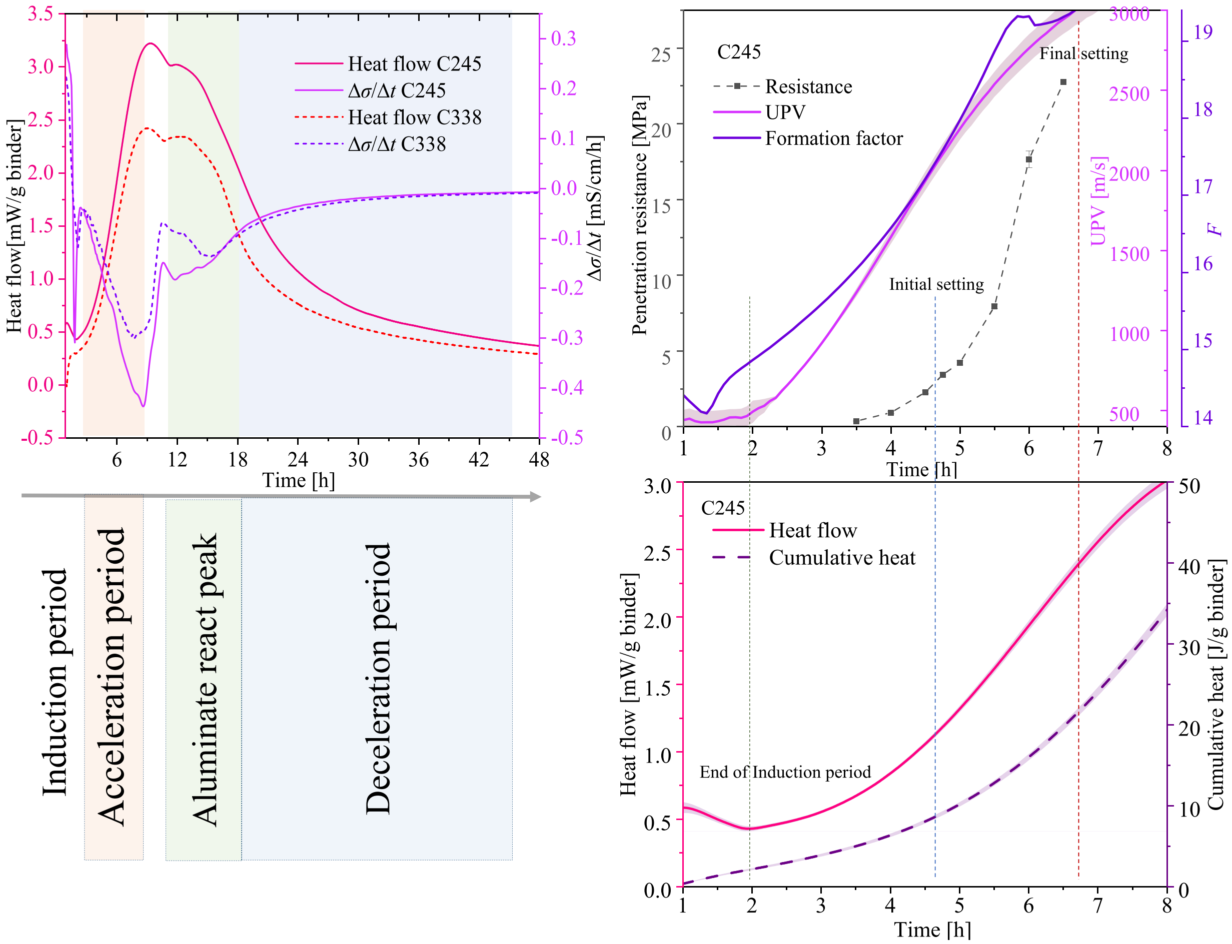

Fig. 8. Detailed comparison between evolution of isothermal calorimetry and electrical conductivity (left side), and its relation to the formation factor, UPV and penetration resistance of C245 (right side).

determined by the development of the yield stress of the cement-based mixture [60]. Only a few of the binders have been reacted to form C-S-H and other hydrates at this stage (see low heat in Fig. 8). Therefore, the stress–strain performance of the fresh mix is partially controlled by C-S-H links and mainly by non-contact colloidal interactions between cement particles [61]. An increase in the network links will increase the elasticity to transform the mechanical properties of matrix from the plastic to elastic state [62], and the semi-solid state is an intermediate state. This implies that the volume of C-S-H and charging state of the particle surfaces are critical for mechanical response during the hardening process. The differences in slopes at two states are more evident between C245 and C338 than that between C145 and C255. The slope of the regression line of C245 and C338 at semi-solid state is only 1/3 to 1/7 of the corresponding slopes in plastic state whereas that ratio is about 1/2 to 1/4 for C145 and C255. As mentioned in the previous section, these differences can be ascribed to discrepancies in the reactivity of binders and *w/b*. However, further investigations are needed to elucidate the underlying mechanism responsible for the different correlations at the semi-solid state.

3.4. Setting, UPV and electrical properties

The percolation theory of consolidation has been extensively applied to understand the mechanics of soil during its drying process [62]. Although Pellenq and Damme [45] highlighted that the setting of cement-based materials was different from soil hardening due to its “wetting” instead of “drying” process, the underlying physics of setting is similar to soil drying due to the formation of solid networks and interactions towards a percolation point for the transition from plastic to elastic state.

Percolation theory based on hardcore/soft-shell model was used to establish a quantitative description of elastic modulus with a certain function during hydration [17]. According to this model, the evolution of UPV from about 4 to 9 h can be described by Eq. (6) with exponent parameter of 2, which is consistent with the experimental results reported in [63].

$$\sqrt{v^2 - v_0^2} = C(t - t_0) \tag{6}$$

where v is the acoustic velocity at curing time t, v_0 is the velocity in the suspension before percolation (herein the UPV of concrete at the initial time is used), C is a free parameter as constant, and t_0 is the time for the percolation of solid network. The evolution of electrical properties during the setting process has the similar tendency as UPV regarding the percolation of solid networks between particles [63]. Correlation between formation factor and evaporable water content has been well described by the percolation theory with a exponent parameter of about 2 [20]. Therefore, Eq. (6) is modified by replacing the acoustic velocity with formation factor to obtain Eq. (7).

$$\sqrt{F^2 - F_0^2} = h(t - t_0) \tag{7}$$

where F is the formation factor at curing time t, F_0 is the formation factor at few minutes after water addition, and h is a free parameter constant.

Fig. 10 shows the regression results by using Eq. (6) and Eq. (7) in a certain time interval to describe correlation between UPV, formation

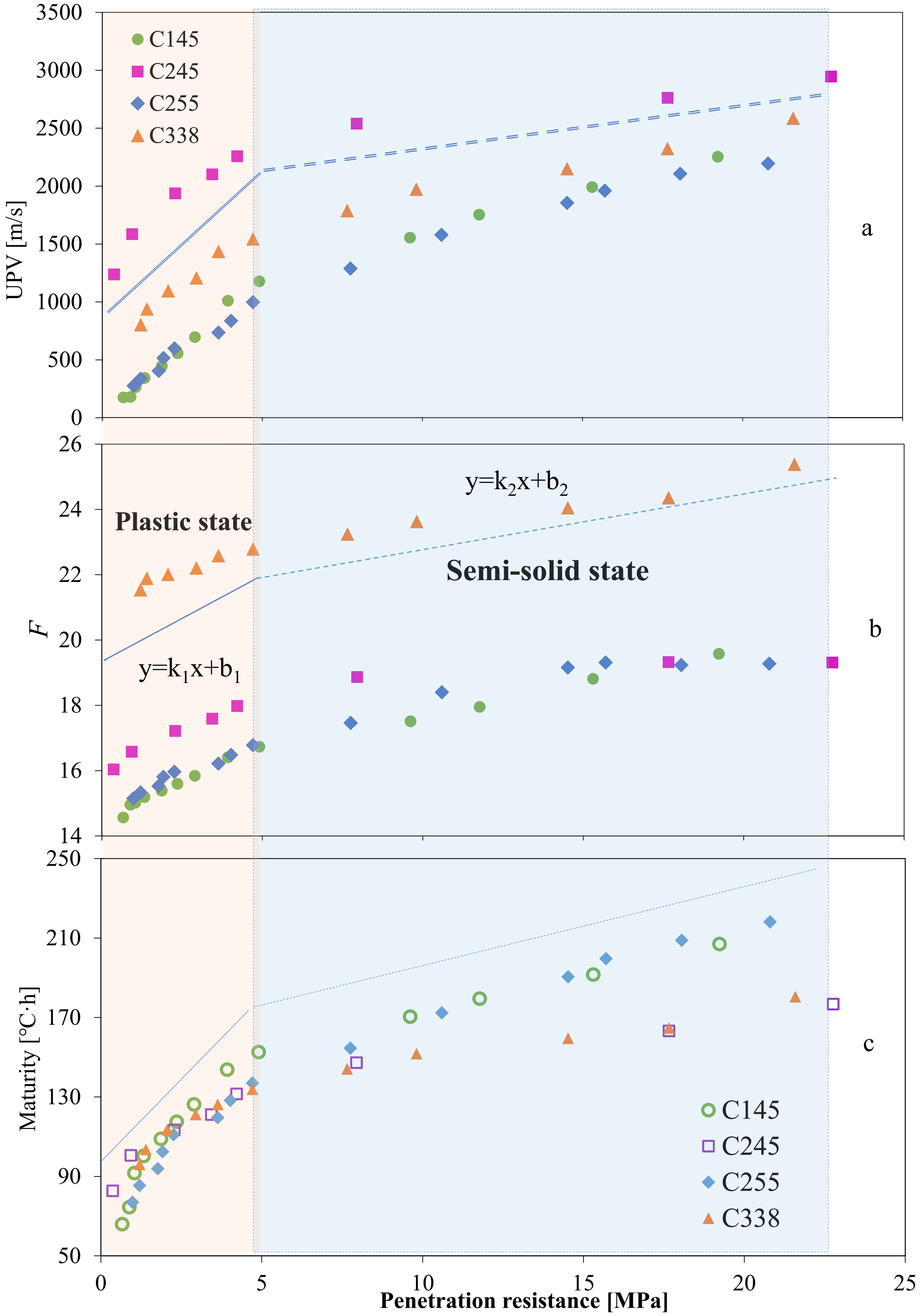

Fig. 9. Quantitative correlation between penetration resistance and UPV, formation factor or maturity.

factor and curing time. The regression part of data from formation factor was selected within a time interval with a good linear correlation before the second inflection (see Fig. 10a). The transition from semi-solid to a solid state can be indicated by inflection point of growth rate of formation factor (*a-F*), which is calculated by dividing formation factor with hydration time [20]. UPV was analyzed in the same way to get the inflection time for growth rate of UPV (*a-UPV*) (Fig. 10c and d).

Table 3 summarizes the regression function, critical time and the setting time of all concrete samples. Fig. 11 presents the correlation between critical time and setting time. Critical time for changing of formation factor can well describe both initial setting and final setting of low carbon concrete mixtures with a linear correlation regardless of temperatures. The inflection time of *a-UPV* can have a similar indication on final setting as formation factor, but the critical time of UPV change seems to have a worse correlation to the initial setting time.

3.5. *After final setting*

3.5.1. *Compressive strength development*

The compressive strength of concrete was tested after final setting to reveal the development of mechanical performance during the hardening process (see Fig. 12). Fly ash binary concrete (C145) has the

Table 2
Regressed parameters between penetration resistance and indices at plastic state and semi-solid state.

Mix ID	Parameters	Plastic state (k_1, b_1)			Semi-solid state (k_2, b_2)		
		Relation to UPV	Relation to *F*	Relation to maturity	Relation to UPV	Relation to *F*	Relation to maturity
C145	*k*	245.78	0.48	19.3	75.27	0.2	4
	b	3.4	14.5	66	831	15.6	131.1
	R^2	1	0.98	0.93	1	1	0.99
C245	*k*	247.2	0.47	11.31	33.73	0.07	2.26
	b	1268.5	16	84.5	2182.9	18	125
	R^2	0.95	0.98	0.94	0.95	0.78	0.97
C255	*k*	181.22	0.4	14.78	76.38	0.17	5.15
	b	124	14.9	69	706.8	16.3	115.3
	R^2	0.98	0.96	0.95	0.98	0.87	0.99
C338	*k*	204.82	0.32	10.15	58.16	0.14	2.53
	b	627.3	21.3	88.8	1325.4	22.1	123.8
	R^2	0.96	0.95	0.95	0.98	0.97	0.98

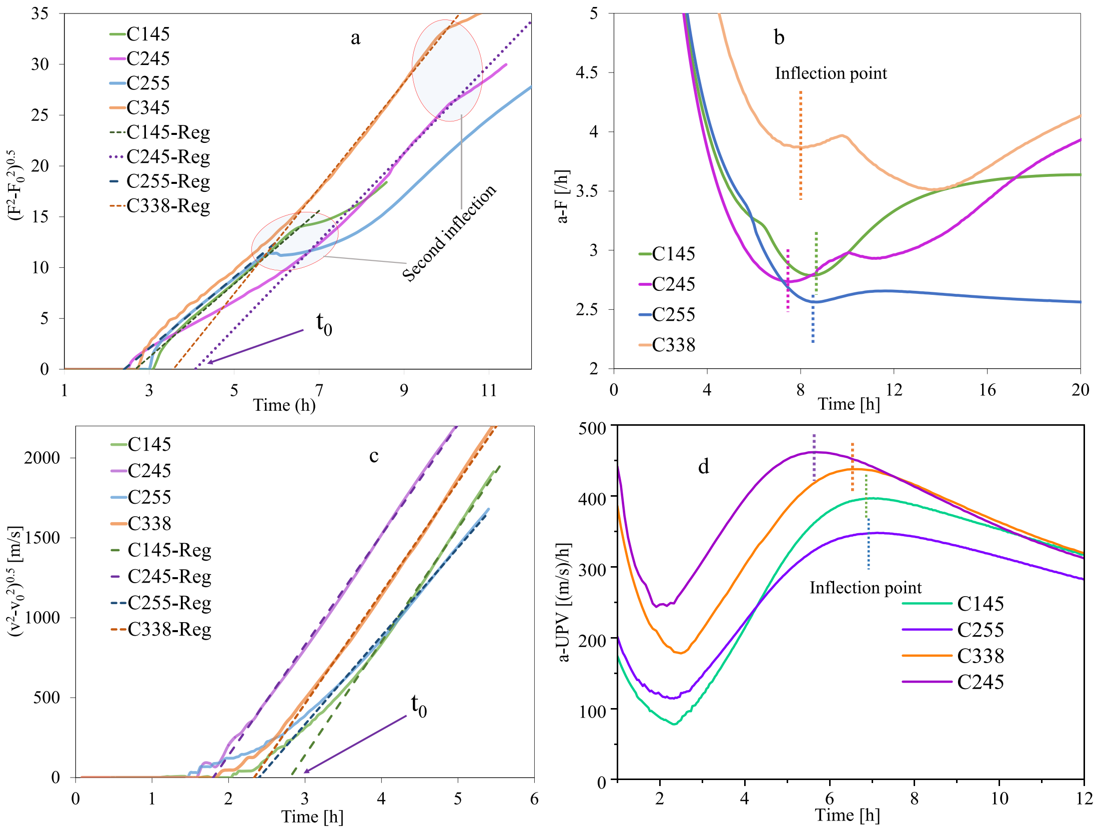

Fig. 10. Setting time assessment of concrete based on the infoection point of UPV and formation factor.

Table 3
Correlation between inflection point, regression function and setting time.

Sample	Regression in selected zone		Critical time [h]				Setting time [h]	
	Eq. (6)	Eq. (7)	t_0 of UPV	t_0 of *F*	Peak of *a-UPV*	Inflection time of *a-F*	Initial setting	Final setting
C145	y = 710x-1990	y = 3.60x-9.64	2.80	2.68	7.00	8.48	3.81	6.82
C245	y = 690x-1242	y = 4.32x-17.64	1.80	4.08	5.67	7.33	4.83	6.56
C255	y = 553x-1326	y = 3.49x-8.42	2.40	2.41	7.25	8.58	3.73	6.97
C338	y = 694x-1622	y = 5.19x-18.50	2.34	3.56	6.64	7.72	4.41	6.31

highest compressive strength at 12 h with a value of 5.9 MPa, and the slag blended concrete have a very similar strength varying from 4.0 to 4.6 MPa at this age. The reason for C145 gaining such a strength value may be ascribed to its highest content of cementitious materials and also probably the curing temperature effect (see the highest maturity in Fig. 5). The strength development from 24 to 168 h is determined by the *w/b* and the reactivity of the SCMs. A lower *w/b* commonly results in a higher compressive strength at this period. Given the same *w/b*, slag reacts faster than fly ash [39,64] so the slag blended mix has a higher strength than the fly ash concrete at early age. Despite with a higher *w/b*, compressive strength of C255 seems to be higher than C145 after 336 h due to the expected higher reactivity of slag compared with fly ash.

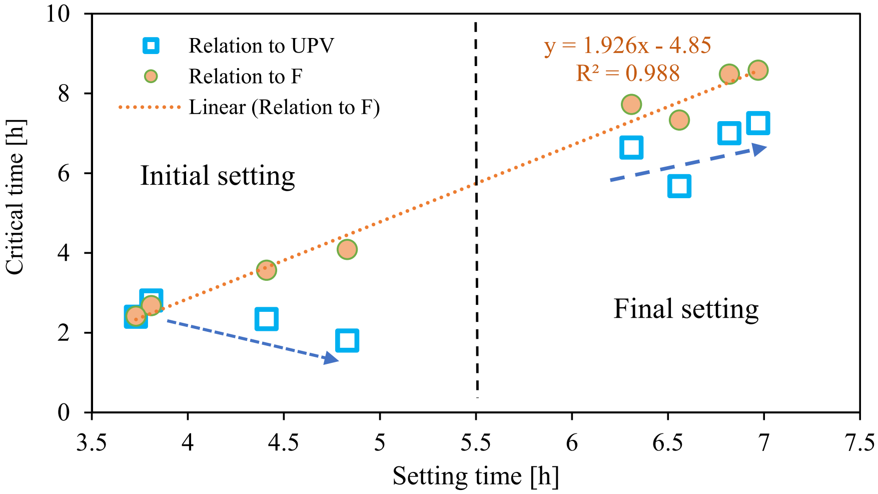

Fig. 11. Correlation between setting time and critical time of the monitored indices.

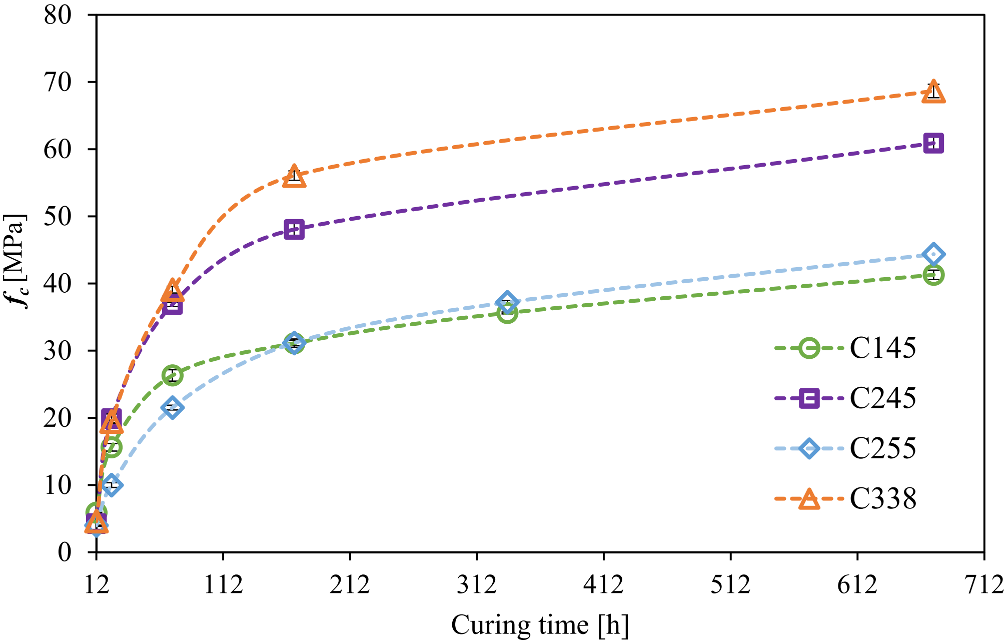

Fig. 12. Development of compressive strength of low carbon concrete after final setting.

Compared with C245, the larger strength development in C338 after 24 h is not only due to the lower *w/b* but also the filler effect of limestone. The chemical interaction of ions with the surface of limestone somehow alters hydration kinetics and phase assemblage. The fine limestone enables nucleation of C-S-H on the surface of calcite and promotes the formation of other phases, such as carboaluminates. Therefore, the addition of an appropriate amount of fine limestone can enhance early strength development [31,65].

3.5.2. Correlation between compressive strength, formation factor, UPV and maturity

Electrical conductivity of cement-based materials under certain temperature is determined by the porosity, ion concentration and connectivity of pore solution [20]. The use of formation factor can exclude the effect of ion concentration in pore solution, so it directly relates to water porosity according to Archie's law [66] as Eq. (8).

$$F = a(\Phi)^{-m} \tag{8}$$

where parameter a is non-uniform constant, m is the shape factor (with an average value of 2 for binders in this study) and Φ is the volume fraction of pores filled with the conductive solution.

This equation describes the volume of pores filled with a conductive liquid, so it may exclude the empty pores and air void in the non-saturated concrete matrix. However, the samples in this study are cured under the sealed condition so the matrix is a naturally saturated condition with limited proportion of empty air voids. It should however be emphasized that in practical utilization, the saturation degree of the matrix should be taken into consideration.

The mechanical performance of porous materials is determined by pore structures inside the matrix. Many empirical functions were proposed to describe the correlation between the porosity and compressive strength of concretes [67,68]. One typical expression is a logarithmic function reported by Schiller [69]:

$$f_c = Kln(\Phi_0/\Phi) \tag{9}$$

where f_c is the compressive strength, K is the constant parameter, and Φ_0 is porosity at which the strength practically vanishes. After substituting Eq. (8) into Eq. (9), we can obtain a logarithmic function for describing the correlation between formation factor and compressive strength as Eq. (10).

$$f_c = K\left(ln\Phi_0 - \frac{lna}{m}\right) + \frac{K}{m}lnF \tag{10}$$

Fig. 13a shows that compressive strength has a linear correlation with ln$F$ having a $R^2 = 0.99$. This quantitative description presents an potential for in-situ monitoring of the strength development of low carbon concretes containing different SCMs. It shows independent on the curing age as well as the binder types. For comparison, the correlation between compressive strength and electrical conductivity of concretes (σ_c) is illustrated in Fig. 13b. Although the R^2 is rather high with 0.96, Fig. 13d illustrates that its deviation is much higher than the relation to formation factor. The primary reason for this phenomenon is the influence of the ionic conductivity of the pore solution on the electrical conductivity of the concrete.

For the scientific description of the relationship between strength and pore size based on physical principles, Luping [70] proposed a model using Griffith's theory to include the average pore radii. Furthermore, Kumar and Bhattacharjee [71] simplified the correlation between porosity and compressive strength as Eq. (11).

$$f_c = \sqrt{\frac{E_0T_0}{\pi}}\,\frac{1-\Phi}{\sqrt{r_m}} \tag{11}$$

where E_0, T_0 and r_m are the modulus of elasticity, specific surface energy of solid and the mean distribution radius, respectively. With the porosity from Eq. (8), we can rewrite Eq. (12) for correlating the strength to formation factor and pore radius.

$$f_c = \frac{K_2}{\sqrt{r_m}}\left[1-\left(\frac{F}{a}\right)^{-\frac{1}{m}}\right] \tag{12}$$

where K_2 is a constant including intrinsic properties of solid (E_0, T_0). For a consolidation packing, the critical radii in porous materials is related to the formation factor as Eq. (13) [72]: Therefore, we can get the correlation between formation factor and strength as Eq. (14).

$$r_m \propto \frac{1}{\sqrt{F}} \tag{13}$$

$$f_c \propto K_2 \cdot F^{\frac{1}{4}} \cdot \left[1-\left(\frac{F}{a}\right)^{-\frac{1}{m}}\right] \tag{14}$$

Fig. 13c shows the regression between $F^{1/m}$ ($m = 2$) and compressive strength, and it is rather reliable with $R^2 = 0.99$. The quantitative expression is established between formation factor and compressive strength as Eq. (15). This expression is also independent on curing time or binder types.

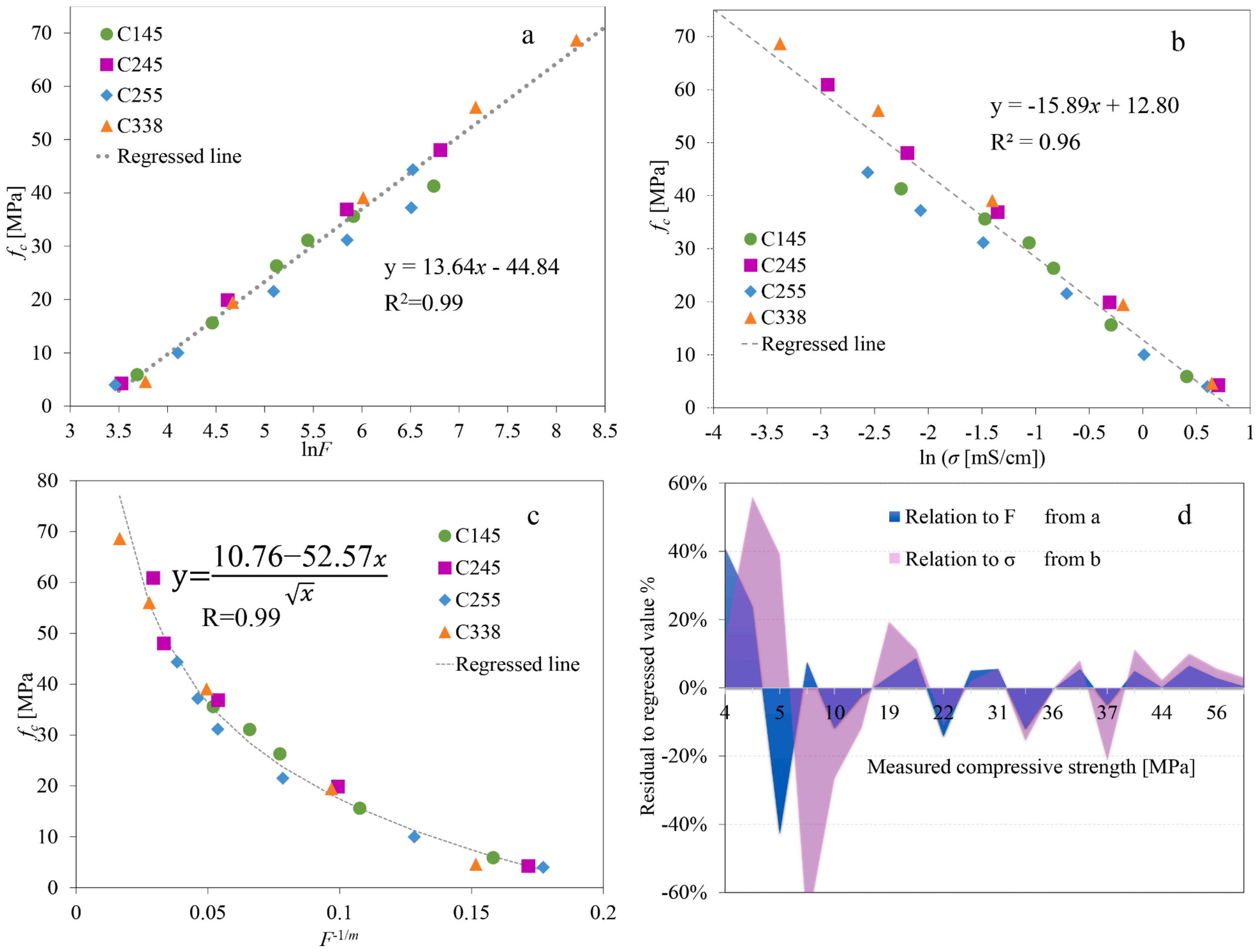

Fig. 13. Quantitative correlations between compressive strength and electrical properties in different functions.

$$f_c = F^{\frac{1}{4}} \times \left(10.76 - 52.57F^{-\frac{1}{2}}\right) = 10.76F^{\frac{1}{4}} - 52.57F^{-\frac{1}{4}} \tag{15}$$

Hereto, two quantitative descriptions have been proposed for the compressive strength in relation to formation factor. Eq. (10) is an empirical correlation, but it is straight forward and simple, so it can be easily used in practice. Correlation in Eq. (14) is deduced by following the physical principle. It is more suitable for scientific understanding but not so easy to be used in practice.

In previous investigations, the compressive strength was widely correlated to UPV [7,9,13,44,73–75] or maturity of concrete mixtures [13,34,36,38]. For highlighting the advantage of the formation factor, the correlations of compressive strength in relation to maturity and UPV have been regressed in Fig. 14. It is obvious that the correlation between maturity and strength is largely dependent on the binder types and *w/b*. The general correlation for all mixtures leads to a very weak exponential relationship with a R^2 of 0.78. Many empirical expressions have been reported for describing correlation between UPV and strength as summarized in [75]. The results in this study can be regressed with an exponential expression as Eq. (16). In which *A* and *B* are constant parameters.

$$f_c = A \cdot e^{B \cdot v} \tag{16}$$

Although the R^2 is 0.96, the data points of C145 and C255 deviate largely from the regression line. In summary, the correlation between formation factor and strength is the best among three indices, which can be applied on-site to monitor the compressive strength development of low carbon concretes regardless of the mixture proportions and environmental temperatures.

4. Conclusions

A reliable non-destructive monitoring approach is essential for promoting the application of various SCMs in the concretes no matter for on-site construction or automated fabrication. This study invented an automated monitoring system for profiling the electrical conductivity of the concrete with the incorporation of SCMs. The embeded temperature sensors allow to simultaneously record the inner temperature at different depths, which is also very useful for normalizing the electrical conductivity to a reference temperature. The credibility of the method is verified by comparing the monitored data with parameters obtained from several traditional methods for testing the hydration, setting time, and compressive strength. The mechanism of monitoring system to map the structural and strength development has been analyzed in detail. The main findings of this study are summarized as follow.

The presented test system can effectively measure the electrical conductivity of hydrating low carbon concretes at different depths by automatic control to avoid polarization and cross-layer interference. Monitored conductivity profiles in time indicates the hydration reactions that happens at the early ages. It can reflect the reaction kinetic of alite and aluminates, which is confirmed by comparison with isothermal calorimetry measurements. An increase in the electrical conductivity during the second aluminate reaction is most likely caused by rise in the concentration of hydroxide ions.

The monitored ultrasonic pulse velocity is a good indicator for the initial setting process of low CO_2 concretes, but its value is dependent on the mixture proportion of concrete especially on the aggregate content. Both formation factor and UPV are good indices for replicating the evolution of the hardening process before final setting. The mechanical response of hydrating concretes can be classified into plastic and semi-solid state with a critical penetration resistance of 4.9 MPa. At each state, a good linear correlation has been established for penetration resistance in relation to UPV, formation factor and maturity, respectively. The evolution of UPV and formation factor has a sudden change during the hardening process, which can be explained by the percolation theory. The inflection time of formation factor correlates linearly to the initial and final setting time of concrete. Blending of fly ash and slag, as well as change of *w/b*, impacts the hardening and strength development of concrete, but this is strongly dependent on the temperature history. The approach and developed device in this study can include all these factors for onsite monitoring of concrete performance.

The parameters from nondestructive test methods reflect the hydration induced structural change and the development of mechanical performance. Although all indices, including electrical conductivity, formation factor, maturity and UPV, can indicate the compressive strength development of low CO_2 concrete with variations in mixture, the formation factor is concluded to the best indicator since it is independent of the binder types, mixing proportion and curing ages. The saturation degree and carbonation of matrix may affect the correlation between the electrical conductivity and performance of concretes. Therefore, it is meaningful for revealing how these factors affect the reliability of this nondestructive system in the future research.

CRediT authorship contribution statement

Liming Huang: Writing – review & editing, Writing – original draft, Visualization, Validation, Software, Methodology, Investigation, Formal analysis, Data curation, Conceptualization. **Luping Tang:** Writing –

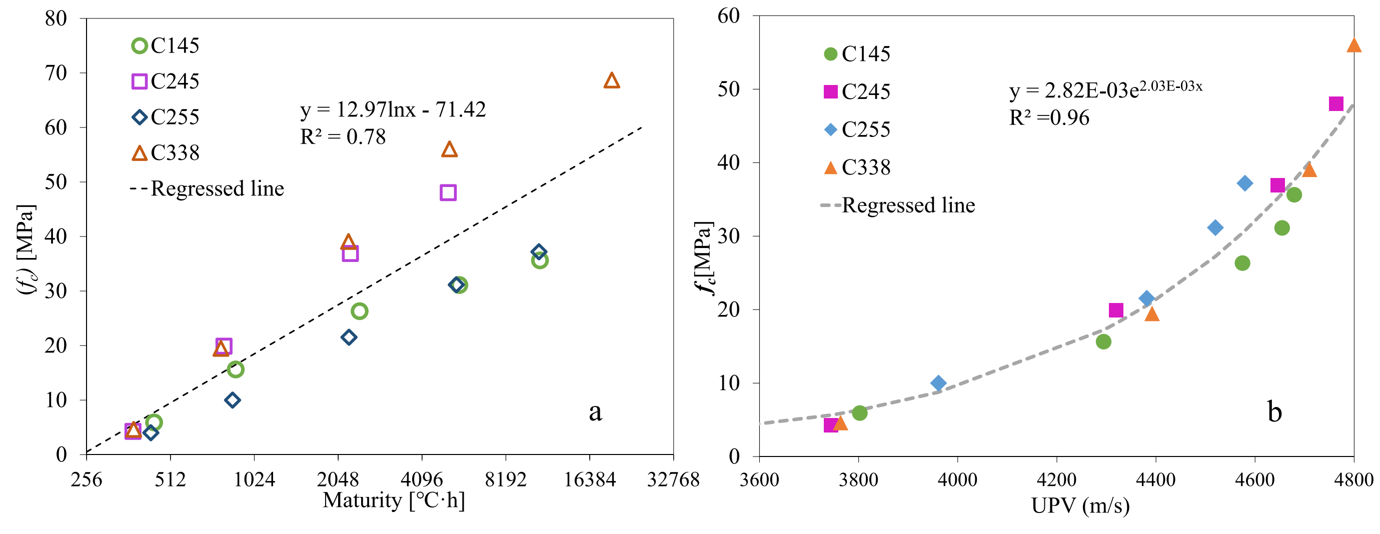

Fig. 14. Quantitative correlations between compressive strength and maturity or UPV.

review & editing, Supervision, Project administration, Methodology, Funding acquisition, Formal analysis, Conceptualization. **Ingemar Löfgren:** Writing – review & editing, Validation, Supervision, Resources, Project administration, Investigation, Funding acquisition. **Nilla Olsson:** Writing – review & editing, Supervision, Resources, Project administration, Investigation, Funding acquisition. **Arezou Baba Ahmadi:** . **Oskar Esping:** Software, Methodology, Investigation, Formal analysis, Data curation. **Yongqiang Li:** Validation, Methodology, Investigation, Formal analysis, Data curation. **Zhenghong Yang:** Writing – review & editing, Supervision, Resources, Project administration, Funding acquisition.

Declaration of Competing Interest

The authors declare that they have no known competing financial interests or personal relationships that could have appeared to influence the work reported in this paper.

Data availability

Data will be made available on request.

Acknowledgements

The authors thank Dr. Shufeng Wang for his nice support in casting the specimens. The authors also appreciate the financial support from Swedish Research Council for Environment, Agricultural Sciences and Spatial Planning FORMAS (2018-01430) and National Key Research and Development Program of China (No. 2018YFD1101002). We also appreciate the partially financial supports from Thomas Concrete Group, SBUF (the construction industry's organization for research and development) and Cementa AB.

References

[1] P.J.M. Monteiro, S.A. Miller, A. Horvath, Towards sustainable concrete, Nature Mater. 16 (2017) 698–699, https://doi.org/10.1038/nmat4930.

[2] G. Habert, S.A. Miller, V.M. John, J.L. Provis, A. Favier, A. Horvath, K.L. Scrivener, Environmental impacts and decarbonization strategies in the cement and concrete industries, Nat. Rev. Earth Environ. 1 (2020) 559–573, https://doi.org/10.1038/s43017-020-0093-3.

[3] N. De Belie, M. Soutsos, E. Gruyaert, eds., Properties of Fresh and Hardened Concrete Containing Supplementary Cementitious Materials: State-of-the-Art Report of the RILEM Technical Committee 238-SCM, Working Group 4, Springer International Publishing, Cham, 2018. https://doi.org/10.1007/978-3-319-70606-1.

[4] L. Reiter, T. Wangler, A. Anton, R.J. Flatt, Setting on demand for digital concrete – Principles, measurements, chemistry, validation, Cem. Concr. Res. 132 (2020), 106047, https://doi.org/10.1016/j.cemconres.2020.106047.

[5] V. Mechtcherine, K. van Tittelboom, A. Kazemian, E. Kreiger, B. Nematollahi, V. N. Nerella, M. Santhanam, G. de Schutter, G. Van Zijl, D. Lowke, E. Ivaniuk, M. Taubert, F. Bos, A roadmap for quality control of hardening and hardened printed concrete, Cem. Concr. Res. 157 (2022), 106800, https://doi.org/10.1016/j.cemconres.2022.106800.

[6] H.W. Reinhardt, ed., Testing during concrete construction: proceedings of the international workshop held by RILEM (the International Union of Testing and Research Laboratories for Materials and Structures) and organized by the Institut für Massivbau, in: Proc. Int. Workshop Held RILEM Int. Union Test. Res. Lab. Mater. Struct., Chapman and Hall, Technical University of Darmstadt, Germany, Mainz, 1990.

[7] V.M. Malhotra (Ed.), Handbook on Nondestructive Testing of Concrete, 2. ed, CRC Press, Boca Raton, 2004.

[8] C. Maierhofer, H.-W. Reinhardt, G. Dobmann, Non-destructive evaluation of reinforced concrete structures: Non-destructive testing methods, Elsevier, 2010.

[9] D. Breysse, Non-destructive assessment of concrete structures: Reliability and limits of single and combined techniques: State-of-the-art report of the RILEM technical committee 207-INR, Springer Science & Business Media, 2012.

[10] X. Tan, A. Abu-Obeidah, Y. Bao, H. Nassif, W. Nasreddine, Measurement and visualization of strains and cracks in CFRP post-tensioned fiber reinforced concrete beams using distributed fiber optic sensors, Autom. Constr. 124 (2021), 103604, https://doi.org/10.1016/j.autcon.2021.103604.

[11] H. Gu, G. Song, H. Dhonde, Y.L. Mo, S. Yan, Concrete early-age strength monitoring using embedded piezoelectric transducers, Smart Mater. Struct. 15 (2006) 1837–1845, https://doi.org/10.1088/0964-1726/15/6/038.

[12] R. Tawie, H.K. Lee, Monitoring the strength development in concrete by EMI sensing technique, Constr. Build. Mater. 24 (2010) 1746–1753, https://doi.org/10.1016/j.conbuildmat.2010.02.014.

[13] T. Voigt, Z. Sun, S.P. Shah, Comparison of ultrasonic wave reflection method and maturity method in evaluating early-age compressive strength of mortar, Cem. Concr. Compos. 28 (2006) 307–316, https://doi.org/10.1016/j.cemconcomp.2006.02.003.

[14] Y. Shimizu, An electrical method for measuring the setting time of portland cement, Mill Sect. Concr. 32 (1928) 111–113.

[15] J. Calleja, New techniques in the study of setting and hardening of hydraulic materials, in, J. Proc. (1952) 525–536.

[16] J. Zhang, E.A. Weissinger, S. Peethamparan, G.W. Scherer, Early hydration and setting of oil well cement, Cem. Concr. Res. 40 (2010) 1023–1033, https://doi.org/10.1016/j.cemconres.2010.03.014.

[17] G.W. Scherer, J. Zhang, J.A. Quintanilla, S. Torquato, Hydration and percolation at the setting point, Cem. Concr. Res. 42 (2012) 665–672, https://doi.org/10.1016/j.cemconres.2012.02.003.

[18] B. Wang, P. Faure, M. Thiéry, V. Baroghel-Bouny, 1H NMR relaxometry as an indicator of setting and water depletion during cement hydration, Cem. Concr. Res. 45 (2013) 1–14, https://doi.org/10.1016/j.cemconres.2012.10.017.

[19] A. Poursaee, W.J. Weiss, An automated electrical monitoring system (AEMS) to assess property development in concrete, Autom. Constr. 19 (2010) 485–490, https://doi.org/10.1016/j.autcon.2009.12.016.

[20] L. Huang, L. Tang, I. Löfgren, N. Olsson, Z. Yang, Real-time monitoring the electrical properties of pastes to map the hydration induced microstructure change in cement-based materials, Cem. Concr. Compos. 132 (2022), 104639, https://doi.org/10.1016/j.cemconcomp.2022.104639.

[21] J.D. Rhoades, P.A.C. Raats, R.J. Prather, Effects of Liquid-phase Electrical Conductivity, Water Content, and Surface Conductivity on Bulk Soil Electrical Conductivity, Soil Sci. Soc. Am. J. 40 (1976) 651–655, https://doi.org/10.2136/sssaj1976.03615995004000050017x.

[22] S.-T. Yi, E.-I. Yang, J.-C. Choi, Effect of specimen sizes, specimen shapes, and placement directions on compressive strength of concrete, Nucl. Eng. Des. 236 (2006) 115–127, https://doi.org/10.1016/j.nucengdes.2005.08.004.

[23] L. Huang, Z. Yang, Early hydration of tricalcium silicate with potassium hydroxide and sulfate from pore solution and solid view, Constr. Build. Mater. 230 (2020), 116988, https://doi.org/10.1016/j.conbuildmat.2019.116988.

[24] J. Fu, A.M. Jones, M.W. Bligh, C. Holt, L.M. Keyte, F. Moghaddam, S.J. Foster, T. D. Waite, Mechanisms of enhancement in early hydration by sodium sulfate in a slag-cement blend – Insights from pore solution chemistry, Cem. Concr. Res. 135 (2020), 106110, https://doi.org/10.1016/j.cemconres.2020.106110.

[25] A. Vollpracht, B. Lothenbach, R. Snellings, J. Haufe, The pore solution of blended cements: a review, Mater. Struct. 49 (2016) 3341–3367, https://doi.org/10.1617/s11527-015-0724-1.

[26] L. Huang, L. Tang, H. Gu, Z. Li, Z. Yang, New insights into the reaction of tricalcium silicate (C3S) with solutions to the end of the induction period, Cem. Concr. Res. 152 (2022), 106688, https://doi.org/10.1016/j.cemconres.2021.106688.

[27] D. Jansen, F. Goetz-Neunhoeffer, C. Stabler, J. Neubauer, A remastered external standard method applied to the quantification of early OPC hydration, Cem. Concr. Res. 41 (2011) 602–608, https://doi.org/10.1016/j.cemconres.2011.03.004.

[28] L. D`Aloia, G. Chanvillard, Determining the ‘“apparent”’ activation energy of concrete Ea—numerical simulations of the heat of hydration of cement, Cem. Concr. Res. 32 (2002) 1277–1289.

[29] X. Pang, L. Sun, F. Sun, G. Zhang, S. Guo, Y. Bu, Cement hydration kinetics study in the temperature range from 15 °C to 95 °C, Cem. Concr. Res. 148 (2021), 106552, https://doi.org/10.1016/j.cemconres.2021.106552.

[30] Y. Briki, M. Zajac, M.B. Haha, K. Scrivener, Impact of limestone fineness on cement hydration at early age, Cem. Concr. Res. 147 (2021), 106515, https://doi.org/10.1016/j.cemconres.2021.106515.

[31] Y. Dhandapani, M. Santhanam, G. Kaladharan, S. Ramanathan, Towards ternary binders involving limestone additions — A review, Cem. Concr. Res. 143 (2021), 106396, https://doi.org/10.1016/j.cemconres.2021.106396.

[32] K.L. Scrivener, B. Lothenbach, N. De Belie, E. Gruyaert, J. Skibsted, R. Snellings, A. Vollpracht, TC 238-SCM: hydration and microstructure of concrete with SCMs: State of the art on methods to determine degree of reaction of SCMs, Mater. Struct. 48 (2015) 835–862, https://doi.org/10.1617/s11527-015-0527-4.

[33] L. Wadsö, An international round robin test on isothermal (conduction) calorimetry for measurement of three-day heat of hydration of cement, Cem. Concr. Res. 79 (2016) 316–322.

[34] N.J. Carino, H.S. Lew, The maturity method: theory and application. Proc. 2001 Struct. Congr. Expo., American Society of Civil Engineers, Reston, Virginia, Washington, D.C., 2001.

[35] J.M. Plowman, A.J. Ockleston, R.H. Mills, J.A. Gard, P. Klieger, T.C. Powers, W. T. Marshall, J.D. McIntosh, Discussion: Maturity and the strength of concrete, Mag. Concr. Res. 24 (1956) 169–183.

[36] C.K. Volz, R.L. Tucker, N.H. Burns, H.S. Lew, Maturity effects on concrete strength, Cem. Concr. Res. 11 (1981) 41–50, https://doi.org/10.1016/0008-8846(81)90007-7.

[37] P. Turcry, A. Loukili, L. Barcelo, J.M. Casabonne, Can the maturity concept be used to separate the autogenous shrinkage and thermal deformation of a cement paste at early age? Cem. Concr. Res. 32 (2002) 1443–1450, https://doi.org/10.1016/S0008-8846(02)00800-1.

[38] J. Zhang, D. Cusson, P. Monteiro, J. Harvey, New perspectives on maturity method and approach for high performance concrete applications, Cem. Concr. Res. 38 (2008) 1438–1446, https://doi.org/10.1016/j.cemconres.2008.08.001.

[39] J. Skibsted, R. Snellings, Reactivity of supplementary cementitious materials (SCMs) in cement blends, Cem. Concr. Res. 124 (2019), 105799, https://doi.org/10.1016/j.cemconres.2019.105799.

[40] M.R.J. Wyllie, A.R. Gregory, G.H.F. Gardner, An experimental investigation of factors affecting elastic wave velocities in porous media, Geophysics 23 (1958) 459–493, https://doi.org/10.1190/1.1438493.

[41] H.K. Lee, K.M. Lee, Y.H. Kim, H. Yim, D.B. Bae, Ultrasonic in-situ monitoring of setting process of high-performance concrete, Cem. Concr. Res. 34 (2004) 631–640, https://doi.org/10.1016/j.cemconres.2003.10.012.

[42] N. Robeyst, E. Gruyaert, C.U. Grosse, N. De Belie, Monitoring the setting of concrete containing blast-furnace slag by measuring the ultrasonic p-wave velocity, Cem. Concr. Res. 38 (2008) 1169–1176, https://doi.org/10.1016/j.cemconres.2008.04.006.

[43] M.S. Mohamed, J. Carette, B. Delsaute, S. Staquet, Applicability of Ultrasonic Measurement on the Monitoring of the Setting of Cement Pastes: Effect of Water Content and Mineral Additions, Adv. Civ. Eng. Mater. 6 (2017) 20160062, https://doi.org/10.1520/ACEM20160062.

[44] J. Zhang, L. Qin, Z. Li, Hydration monitoring of cement-based materials with resistivity and ultrasonic methods, Mater. Struct. 42 (2009) 15–24, https://doi.org/10.1617/s11527-008-9363-0.

[45] R.-J.-M. Pellenq, H. Van Damme, Why does concrete set?: the nature of cohesion forces in hardened cement-based materials, MRS Bull. 29 (2004) 319–323, https://doi.org/10.1557/mrs2004.97.

[46] E. Berodier, K. Scrivener, Understanding the Filler Effect on the Nucleation and Growth of C-S-H, J. Am. Ceram. Soc. 97 (2014) 3764–3773, https://doi.org/10.1111/jace.13177.

[47] R.C. Pinto, K.C. Hover, Application of maturity approach to setting times, Mater. J. 96 (1999) 686–691.

[48] D.P. Bentz, Activation energies of high-volume fly ash ternary blends: Hydration and setting, Cem. Concr. Compos. 53 (2014) 214–223, https://doi.org/10.1016/j.cemconcomp.2014.06.018.

[49] R.C. Tank, N.J. Carino, Rate constant functions for strength development of concrete, Mater. J. 88 (1991) 74–83.

[50] A. Schöler, B. Lothenbach, F. Winnefeld, M.B. Haha, M. Zajac, H.-M. Ludwig, Early hydration of SCM-blended Portland cements: A pore solution and isothermal calorimetry study, Cem. Concr. Res. 93 (2017) 71–82, https://doi.org/10.1016/j.cemconres.2016.11.013.

[51] S. Dittrich, J. Neubauer, F. Goetz-Neunhoeffer, The influence of fly ash on the hydration of OPC within the first 44h—A quantitative in situ XRD and heat flow calorimetry study, Cem. Concr. Res. 56 (2014) 129–138, https://doi.org/10.1016/j.cemconres.2013.11.013.

[52] E. Nägele, The zeta-potential of cement, Cem. Concr. Res. 15 (1985) 453–462.

[53] D. Lowke, C. Gehlen, The zeta potential of cement and additions in cementitious suspensions with high solid fraction, Cem. Concr. Res. 95 (2017) 195–204, https://doi.org/10.1016/j.cemconres.2017.02.016.

[54] W.J. McCarter, T.M. Chrisp, G. Starrs, A. Adamson, P.A.M. Basheer, S. V. Nanukuttan, S. Srinivasan, C. Green, Characterization of physio-chemical processes and hydration kinetics in concretes containing supplementary cementitious materials using electrical property measurements, Cem. Concr. Res. 50 (2013) 26–33, https://doi.org/10.1016/j.cemconres.2013.03.008.

[55] C. Hesse, F. Goetz-Neunhoeffer, J. Neubauer, A new approach in quantitative in-situ XRD of cement pastes: Correlation of heat flow curves with early hydration reactions, Cem. Concr. Res. 41 (2011) 123–128, https://doi.org/10.1016/j.cemconres.2010.09.014.

[56] B. Kolani, L. Buffo-Lacarrière, A. Sellier, G. Escadeillas, L. Boutillon, L. Linger, Hydration of slag-blended cements, Cem. Concr. Compos. 34 (2012) 1009–1018, https://doi.org/10.1016/j.cemconcomp.2012.05.007.

[57] J.T. Kolawole, R. Combrinck, W.P. Boshoff, Shear rheo-viscoelasticity approach to the plastic cracking of early-age concrete, Cem. Concr. Res. 135 (2020), 106127, https://doi.org/10.1016/j.cemconres.2020.106127.

[58] B. Dolinar, M. Miŝiĉ, L. Trauner, Correlation between surface area and Atterberg limits of fine-grained soils, Clays Clay Miner. 55 (2007) 519–523, https://doi.org/10.1346/CCMN.2007.0550506.

[59] B.M. Das, Advanced soil mechanics, Fifth edition, CRC Press, Taylor & Francis Group, Boca Raton, 2019.

[60] D. Lootens, P. Jousset, L. Martinie, N. Roussel, R.J. Flatt, Yield stress during setting of cement pastes from penetration tests, Cem. Concr. Res. 39 (2009) 401–408, https://doi.org/10.1016/j.cemconres.2009.01.012.

[61] N. Roussel, G. Ovarlez, S. Garrault, C. Brumaud, The origins of thixotropy of fresh cement pastes, Cem. Concr. Res. 42 (2012) 148–157, https://doi.org/10.1016/j.cemconres.2011.09.004.

[62] S.S. Vi͡alov, Rheological fundamentals of soil mechanics, Elsevier ; Distributors for the United States and Canada, Elsevier Science Pub. Co, Amsterdam ; New York : New York, N.Y, 1986.

[63] A. Boumiz, C. Vernet, F.C. Tenoudji, Mechanical properties of cement pastes and mortars at early ages: Evolution with time and degree of hydration, Adv. Cem. Bas. Mat. 3 (1996) 94–106.

[64] Z. Giergiczny, Fly ash and slag, Cem. Concr. Res. 124 (2019), 105826, https://doi.org/10.1016/j.cemconres.2019.105826.

[65] S. Adu-Amankwah, M. Zajac, C. Stabler, B. Lothenbach, L. Black, Influence of limestone on the hydration of ternary slag cements, Cem. Concr. Res. 100 (2017) 96–109, https://doi.org/10.1016/j.cemconres.2017.05.013.

[66] G.E. Archie, The Electrical Resistivity Log as an Aid in Determining Some Reservoir Characteristics, Trans. AIME 146 (1942) 54–62, https://doi.org/10.2118/942054-G.

[67] A.M. Brandt, Cement-based composites: materials, mechanical properties and performance, CRC Press, 2005.

[68] C. Lian, Y. Zhuge, S. Beecham, The relationship between porosity and strength for porous concrete, Constr. Build. Mater. 25 (2011) 4294–4298, https://doi.org/10.1016/j.conbuildmat.2011.05.005.

[69] K.K. Schiller, Strength of porous materials, Cem. Concr. Res. 1 (1971) 419–422, https://doi.org/10.1016/0008-8846(71)90035-4.

[70] T. Luping, A study of the quantitative relationship between strength and pore-size distribution of porous materials, Cem. Concr. Res. 16 (1986) 87–96, https://doi.org/10.1016/0008-8846(86)90072-4.

[71] R. Kumar, B. Bhattacharjee, Porosity, pore size distribution and in situ strength of concrete, Cem. Concr. Res. 33 (2003) 155–164, https://doi.org/10.1016/S0008-8846(02)00942-0.

[72] A.S. Ziarani, R. Aguilera, Pore-throat radius and tortuosity estimation from formation resistivity data for tight-gas sandstone reservoirs, J. Appl. Geophys. 83 (2012) 65–73, https://doi.org/10.1016/j.jappgeo.2012.05.008.

[73] G. Trtnik, F. Kavčič, G. Turk, Prediction of concrete strength using ultrasonic pulse velocity and artificial neural networks, Ultrasonics 49 (2009) 53–60, https://doi.org/10.1016/j.ultras.2008.05.001.

[74] H.Y. Qasrawi, Concrete strength by combined nondestructive methods simply and reliably predicted, Cem. Concr. Res. 30 (2000) 739–746, https://doi.org/10.1016/S0008-8846(00)00226-X.

[75] D. Breysse, Nondestructive evaluation of concrete strength: An historical review and a new perspective by combining NDT methods, Constr. Build. Mater. 33 (2012) 139–163, https://doi.org/10.1016/j.conbuildmat.2011.12.103.